Time-of-day effects of cancer drugs revealed by high-throughput deep phenotyping

Running title: Time-of-day effects of drugs

Authors: Carolin Ector[1,2], Christoph Schmal[3], Jeff Didier[4], Sébastien De Landtsheer[4], Anna-Marie Finger[5,6], Francesca Müller-Marquardt[1,7], Johannes Schulte[8,9], Thomas Sauter[4], Ulrich Keilholz[1,10], Hanspeter Herzel[3,11], Achim Kramer[5], Adrián E. Granada*[1,10]

First author: Carolin Ector || **Corresponding author:** adrian.granada@charite.de

Affiliations:

1. Charité Comprehensive Cancer Center, Charité – Universitätsmedizin Berlin, Charitéplatz 1, 10117 Berlin, Germany.
2. Faculty of Life Sciences, Humboldt-Universität zu Berlin, Invalidenstraße 42, 10115 Berlin, Germany.
3. Institute for Theoretical Biology, Humboldt-Universität zu Berlin, Philippstraße 13, 10115 Berlin, Germany.
4. Department of Life Sciences and Medicine, University of Luxembourg, 2, Avenue de l'Université, L-4365 Esch-sur-Alzette, Luxembourg.
5. Institute for Medical Immunology, Charité – Universitätsmedizin Berlin, Charitéplatz 1, 10117 Berlin, Germany.
6. Present address: Department of Anatomy, University of California, San Francisco, 513 Parnassus Avenue HSW 1330, San Francisco, CA 94143-0452, USA.
7. Present address: Institute of Research for Development, University of Montpellier, 911 Av. Agropolis, 34394 Montpellier, France.
8. Department of Pediatric Oncology, Hematology and Stem Cell Transplantation, Charité – Universitätsmedizin Berlin, Charitéplatz 1, 10117 Berlin, Germany.
9. Present address: Clinic for Pediatrics and Adolescent Medicine, Universitätsklinikum Tübingen, Hoppe-Seyler-Str. 1, 72076 Tübingen, Germany.
10. German Cancer Consortium (DKTK), Berlin, Germany.
11. Charité – Universitätsmedizin Berlin, Charitéplatz 1, 10117 Berlin, Germany.

Author contributions:
C.E., A.K., and A.E.G. conceived and planned the experiments. C.E. performed the experiments. F.M.M. performed bioluminescence recordings of three cell lines. C.E., C.S., J.D., and S.D.L. analyzed the data. A.M.F. and A.K. supported in the planning and implementation of the bioluminescence recordings. C.E., C.S., A.M.F., J.D., S.D.L., J.S., T.S., U.K, H.H., A.K., and A.E.G. contributed to the interpretation of the results. C.E. and A.E.G wrote the manuscript. All authors provided critical feedback and helped shape the research and manuscript.

Keywords: circadian clock, drug sensitivity, systems biology, chronopharmacology.

Abbreviations:
5-FU, 5-fluorouracil; AC, autocorrelation; ATCC, American type culture collection; BL1, basal-like1; BL2, basal-like2; BMAL1, brain and muscle arnt-like protein-1; CI, confidence interval; CLOCK, circadian locomotor output cycles protein kaput; CRY, cryptochrome; CWT, continuous wavelet transform; dKO, double-knockout; DMEM, Dulbecco's Modified Eagle Medium; DMSO, dimethyl sulfoxide; DWT, discrete wavelet transform; EGF, epidermal growth factor; EP, epithelial; GR, growth rate inhibition; LDA, linear discriminant analysis; Luc, luciferase; MES, mesenchymal; mTOR, mammalian target of rapamycin; NLS, nuclear localization sequence; PARP, poly ADP ribose polymerase; PCA, principal component analysis; PER2, period2; PI3K, phosphatidylinositol 3-kinase/alpha serine/ threonine-protein kinase; ROR, RAR-related orphan receptor; RPMI, Roswell Park Memorial Institute medium; SCN, suprachiasmatic nucleus; sKO, single-knockout; TNBC, triple-negative breast cancer; ToD, time-of-day; TPM, transcripts per million.

Abstract

The circadian clock, a fundamental biological regulator, governs essential cellular processes in health and disease. Circadian-based therapeutic strategies are increasingly gaining recognition as promising avenues. Aligning drug administration with the circadian rhythm can enhance treatment efficacy and minimize side effects. Yet, uncovering the optimal treatment timings remains challenging, limiting their widespread adoption. In this work, we introduce a novel high-throughput approach integrating live-imaging and data analysis techniques to deep-phenotype cancer cell models, evaluating their circadian rhythms, growth, and drug responses. We devised a streamlined process for profiling drug sensitivities across different times of the day, identifying optimal treatment windows and responsive cell types and drug combinations. Finally, we implement multiple computational tools to uncover cellular and genetic factors shaping time-of-day drug sensitivity. Our versatile approach is adaptable to various biological models, facilitating its broad application and relevance. Ultimately, this research leverages circadian rhythms to optimize anti-cancer drug treatments, promising improved outcomes and transformative treatment strategies.

Introduction

The circadian clock is a central regulator of multiple physiological and behavioral processes found in cyanobacteria, plants, fungi, and animals. In mammals, the hierarchical organization of the circadian system ensures coordinated biological rhythms from the level of the individual cell to whole organism level[1]. Primate and mouse studies showed that protein-coding genes are rhythmically expressed in a tissue-specific by up to 80% and 40%, respectively[2,3]. These clock-controlled genes regulate key biological processes such as metabolism[4,5], cell proliferation[6], immune response[7], DNA repair and apoptosis[8].

Disruption of the circadian system is classified as a carcinogen and is associated with multiple cancer subtypes[9-12]. Cancer hallmarks such as sustained proliferation and metastasis[13,14] have been linked to the circadian clock[15,16] and patients with mutations in circadian clock genes exhibit lower survival rates[17-19]. Beyond its role in cancer development, the circadian clock directly interacts with therapeutic targets that affect drug responses[19-21]. Consistent with these observations, recent works have shown that administration of chemotherapeutic agents aligned with the circadian rhythm change their degree of efficacy throughout the day[20,22-24]. Despite the broad recognition of the benefits of circadian-based drug treatments[22,25,26], an efficient strategy to identify optimal treatment times remains elusive, creating a bottleneck in the implementation. In addition, the mechanisms shaping time-of-day (ToD) sensitivity profiles remain widely unknown.

Here, we introduce a novel method for the thorough characterization of time-of-day responses in tumor and healthy tissue cell models (**Fig.1**). Using an array of experimental and data analysis methods we perform a deep-phenotyping of the critical cellular factors underlying time-of-day responses, i.e., the circadian clock strength, growth dynamics and drug response features. We then deploy a new high-throughput strategy to obtain ToD profiles in a panel of drugs and cell line models. Comparing tumor versus non-tumor ToD profiles provides candidate treatment timings to increase efficacy and reduce toxicity. We subsequently integrate our dataset with publicly available gene-expression databases to rigorously address three fundamental questions in the field of circadian pharmacology, known as chronopharmacology. These questions are: (A) what is the optimal time-of-day for drug treatment? (B) which cell subtype benefits the most from a circadian-aligned drug treatment? and (C) how do cellular features shape time-of-day profiles? Finally, we define a chronotherapeutic index, ranking

93 cellular models and drug agents that stands to gain the most benefit from circadian-based
94 treatments.
95

96 Results

97 Deep circadian phenotyping in cancer cell models

98 Despite the increasing recognition of the role of the circadian clock in cancer progression and
99 treatment response, the extent to which different cancer subtypes maintain circadian
100 rhythmicity remains poorly understood. To address this and quantitatively characterize the
101 degree of rhythmicity of cancer cell models, we implement an approach that integrates
102 recordings of circadian clock activity with comprehensive time-series analysis techniques, as
103 depicted in **Fig. 2a**. To robustly characterize the circadian clock molecular network, we
104 monitored the positive and negative feedback arms of the molecular clock using a combination
105 of two circadian luciferase reporters for *Bmal1* and *Per2* (**Fig. 2b**). In **Fig. 2c** we show
106 representative raw luciferase signals from the breast cancer cell line MDAMB468, and the
107 corresponding detrended and normalized signals[27]. As expected for a robust functional clock
108 network, *Bmal1* and *Per2* signals show stable anti-phasic expression patterns throughout the
109 recording (**Fig. 2c** and **Supplementary Fig. 1a,b)**.

110 Circadian clock strength varies in cancer and healthy cell models

111 Following the acquisition of *Bmal1* and *Per2* expression dynamics, we conducted a
112 comprehensive circadian phenotyping of the signals. To accurately capture different aspects of
113 the circadian clock dynamics, we implemented a strategy that integrates three complementary
114 time-series analysis techniques, i.e., autocorrelation (AC), continuous wavelet transform
115 (CWT), and multiresolution analysis (MRA). The rationale behind using this complementary
116 analysis is to harness the strengths of each technique; AC for identifying stable temporal
117 features, CWT for revealing time-dependent amplitude and period changes, and MRA for
118 extracting multi-scale features, ensuring a comprehensive understanding of the signal
119 dynamics. Using this approach we screened a broad panel of cell models, including non-
120 malignant breast epithelial MCF10A, cancer cell models of various entities (breast cancer,
121 neuroblastoma, and sarcoma) as well as two knockout variants of osteosarcoma U-2 OS cells

122 with a single deletion in the circadian clock gene *Cry1* (U-2 OS sKO) or paired with a deletion
123 in the *Cry2* locus[28] (U-2 OS dKO).
124 Autocorrelation is a robust method for estimating the periodic quality of a signal, particularly
125 for time-series whose properties remain stable over time, known as stationary signals.
126 Calculating the autocorrelation function from each recording provides the strength and period
127 values, obtained from the second peak ordinate and abscissa (lag), respectively (**Fig. 2d**). This
128 analysis showed a wide range of circadian strengths across models with the U-2 OS wild-type
129 ranking highest with a median autocorrelation value of 0.74, whereas U-2 OS sKO and U-2 OS
130 dKO variants ranked lowest with median correlation values of -0.04 (p= 7.7 $\times 10^{-12}$) and 0.09
131 (p=1.4$\times 10^{-10}$), respectively (**Fig. 2e**). Heterogeneity between and within cancer types was
132 further observed for the oscillation period ranging from short periods of ~21 h in HCC1806
133 and U-2 OS sKO cells (p=n.s.) to longer periods of ~26 h in MDAMB468 and MCF10A cells.
134 U-2 OS dKO (34.8 h, p=8.2$\times 10^{-5}$) and the neuroblastoma cell line SH-SY5Y (39.2 h) showed
135 periods well above the circadian range and were excluded from this analysis (**Fig. 2f**).
136 Consistent with these results, detrended signal traces of the different cell models and additional
137 breast cancer cell lines indicate high variability in circadian clock signals across the models
138 tested (**Supplementary Fig. 1c**).
139 To capture non-stationary features of the circadian signals, such as unstable periods and
140 fluctuating amplitudes, we implemented continuous wavelet transform, a prevalent technique
141 for analyzing dynamic temporal signals[29]. **Fig. 2g** shows a CWT power spectrum heatmap of
142 *Bmal1* signal from the MDAMB468 example. The heatmap displays signal components (0–40
143 h period) over the 120-h recording, color-coded by relative power (see **Methods**). Time-
144 connected regions of high relative power mark the signal's main oscillatory component,
145 referred to as ridge. Strong signals exhibit continuous long ridges whereas weaker signals have
146 short and discontinuous ridges. As a complementary measure of clock strength, we quantified
147 the ridge length from all our recordings. Our analysis shows that U-2 OS cells have a well-
148 maintained clock with a median ridge length of 4.1 days, closely followed by MCF7,
149 MDAMB468 and MCF10A cells (3.4–3.8 days). U-2 OS sKO and dKO cells showed ridges
150 shorter than two days (1.9 days [p=5.7$\times 10^{-3}$] and 1.5 days [p=4.8$\times 10^{-4}$], respectively) (**Fig.
151 2h**).
152 While both, autocorrelation and continuous wavelet transform, provide insights into the most
153 significant signal component, they do not quantify how the signal is distributed among non-

154 circadian frequencies. To obtain more comprehensive signal information and an analogous
155 signal-to-noise metric, we next implemented multiresolution analysis. MRA involves
156 decomposing the detrended signal into four distinct component bands, namely the noise (1–4
157 h), ultradian (4–16 h), circadian (16–32 h) and infradian (32–48 h) components (see **Methods**).
158 In **Fig. 2i** we present an example of MDAMB468 *Bmal1*-Luc where 75.9% of the signal is in
159 the circadian range, 4.7% in the noise and the remaining 19.4% in the ultradian or infradian
160 range. To obtain an analogous signal-to-noise measure of all recorded cell models, we plotted
161 the circadian component ("circadianicity") versus the noise component and observed a broad
162 range of ratios (**Fig. 2j**). Consistent with our previous analysis, U-2 OS cells show strong
163 circadian signal with the lowest noise levels (<1%) and the highest proportion of circadian
164 components (~93%) for both reporters. Knockout of *Cry1* or *Cry1/Cry2* reduced the circadian
165 component to 59% (p=5.8×10^{-6}) and 40% (p=2.0×10^{-8}), respectively, while increasing the
166 noise component by 5.8-fold in the single knockout and by 209-fold in the double knockout.
167 This signal-to-noise analysis map indicates that signals from the *Per2*-reporter were slightly
168 more circadian and less noisy than those from the *Bmal1*-reporter (**Fig. 2j** and **Supplementary**
169 **Fig. 1d**). *Bmal1* and *Per2* exhibit unique oscillatory patterns, reflecting distinct biological
170 pathways within the circadian clock system. Their individual behaviors might offer valuable
171 insights into the functionality of the circadian rhythm. To streamline our analysis and facilitate
172 comparison, we averaged the values of *Bmal1* and *Per2* in **Fig. 2b, e, h, and k**. However, for
173 a more detailed examination, separate analyses for each can be found in **Supplementary**
174 **Figure 1e and f**.
175 Finally, to obtain a global strength metric, we normalized each circadian parameter to its
176 respective maximum value across all tested cell line models and computed the mean,
177 facilitating a gradual ranking of cell models from low to high circadian strength (**Fig. 2k**, see
178 **Methods**).
179 In summary, by using a multi-faceted approach to characterize circadian rhythms in the
180 different models tested, we identified heterogeneous circadian clock phenotypes, suggesting a
181 strong clock in U-2 OS, MCF7, MDAMB468 and MCF10A cells and an impaired but present
182 clock in GIMEN and HCC1806 cells. These results challenge the common expectation that
183 most cancer cells have a weak clock and underscore the significance of defining gradual
184 metrics of circadian strength in a model-specific manner.
185

186 ## Growth and drug response dynamics in cancer cell models

187 Together with circadian potency, cell growth dynamics and how cells respond to drug treatment
188 in time is expected to influence responses along the day. Thus, we next evaluated growth
189 characteristics and drug sensitivities across a spectrum of drug and cell line models. To
190 showcase our approach's ability in detecting within-subtype differences, we examined nine cell
191 lines of the triple-negative breast cancer (TNBC) subtype alongside the non-malignant
192 MCF10A breast cell model. The TNBC cell lines were analyzed across several molecular
193 subtypes as classified by Lehmann *et al.*, specifically the basal-like 1 (BL1), basal-like 2 (BL2),
194 and mesenchymal (MES) TNBC subtypes. Growth and drug sensitivity assays in cancer models
195 often rely on single time point measurements (e.g., ATP-based viability and replating assays)
196 that provide a time-averaged snapshot. However, cancer cells respond dynamically to drugs,
197 with temporally evolving effects, so conclusions drawn from single time point data can
198 potentially mask the true effects of drugs. To accurately capture the dynamics of growth and
199 drug response, we implemented a time-resolved live-cell imaging setup, directly counting cell
200 nuclei in a fluorescence channel, while simultaneously evaluating confluency in the
201 complementary brightfield channel (**Fig. 3a**). **Fig. 3b** shows representative snapshots of both
202 imaging channels from MDAMB468 cells under untreated conditions. Frame-by-frame
203 quantification provides growth trajectories for each cell model tested (**Supplementary Fig.
204 2a)**, with MDAMB468 cells showing a 5.3-fold increase in growth and reaching approximately
205 100% confluency after 4 days (**Fig. 3c**). Quantification of doubling times (DTs) calculated
206 from confluency and cell numbers correlated well across the 10 cell line models tested
207 (R^2=0.69) (**Supplementary Fig. 2b**). Upon examining the normalized cell number trajectories,
208 we observed substantial variability in growth across the cell line models, ranging from
209 approximately 2- to 16-fold over the 4-day recordings (**Fig. 3d**). To capture growth signatures
210 from the entire recording, we fitted an exponential function to each time series and obtained
211 the growth rate k for each trajectory (**Fig. 3e**). As expected, cell number growth rates and
212 doubling times exhibit a strong anticorrelation (R^2=0.83) (**Fig. 3f** and **Supplementary Fig. 2c**).
213 Next, we studied the response of the cancer cell models upon treatment with a panel of seven
214 drugs targeting a broad range of mechanisms and pathways, i.e., the DNA synthesis inhibitors
215 5-FU and doxorubicin, mitosis-inhibiting alisertib and paclitaxel, the PI3K/AKT/mTOR
216 inhibitor torin2, as well as cisplatin and olaparib which target the DNA damage response
217 (DDR) pathway (**Fig. 3g**). We then tracked responses to a broad range of drug concentrations,

218 as exemplified in **Fig. 3h** by MDAMB468's olaparib treatment. Here, doses up to 1.5 µM
219 resulted in slightly slower growth relative to the control, while 6.3 µM of olaparib significantly
220 hindered growth, and ≥25 µM led to total inhibition and cell death. Fitting an exponential
221 function to growth curves yielded positive growth rate values for weak doses while higher
222 doses resulted in negative growth rates, indicating population decline. Using this approach, we
223 next quantified the response and stratified all tested cell lines and drugs.
224

225 Multi-parametric evaluation of drug sensitivity reveals heterogeneity 226 between and within models

227 Accurate assessment of drug effects is essential for identifying exploitable weaknesses in
228 cancer treatments. Traditional drug sensitivity metrics, like the IC_{50} (the drug concentration
229 that reduces cell counts by 50% relative to the control), can be greatly influenced by factors
230 such as the assay duration and the number of cell divisions between drug administration and
231 final evaluation of drug sensitivity. These factors can inadvertently introduce artefactual
232 correlations and lead to misinterpretations of drug sensitivity results. To obtain robust drug
233 sensitivity metrics, we employed the normalized growth rate inhibition (*GR*) approach as
234 described by Hafner *et al.*[30]. Here, growth rates under treated and untreated conditions are
235 compared and normalized to a single cell division. Fitting a dose-response equation to *GR*
236 values yields five drug sensitivity parameters, namely, the concentrations at half-maximal
237 effect (GEC_{50}) and at which GR=0.5 (GR_{50}), the drug effect at infinite concentration (GR_{inf}),
238 the steepness of the sigmoidal fit (*Hill coefficient*), and the area over the curve (GR_{AOC}) (**Fig.
239 3i**). Moreover, the *GR* value directly reflects cellular response phenotypes, indicating partial
240 growth inhibition for values between 0 and 1, complete cytostasis for a value of 0, and
241 signifying cell death in the range from 0 to -1. Interestingly, when the same cell line was treated
242 with different cancer drugs at their respective concentration evoking a saturating GR_{inf} response
243 distinct drug-dependent trajectories emerged (**Fig. 3j**). This underscores the importance of a
244 time-resolved approach for characterizing drug sensitivity across different drugs and,
245 accordingly, across distinct cell line models.
246 We next compared a subset of drug-sensitivity metrics and cell line models for the different
247 drugs tested (**Fig. 3k–m**). While most drugs were able to induce death in the subset of cell lines
248 to varying degrees, we identified three drugs that resulted in partial growth inhibition of

249 HCC1806, namely olaparib, 5-FU and alisertib (**Fig. 3k**). Hierarchical clustering of GR_{inf}
250 values revealed a grouping of the two TNBC cell lines and while this clustering was maintained
251 for the GEC_{50} values (**Fig. 3l**), the Hill coefficient resulted in a different clustering of the cell
252 lines (**Fig. 3m**). To explore the potential relationships between various sensitivity metrics, we
253 combined data from multiple drugs and cell models and computed cross-correlations, revealing
254 significant associations among GEC_{50}, GR_{50}, and EC_{50} values ($p \leq 0.0001$) (**Fig. 3n**).
255 Additionally, significant yet less pronounced correlations emerged between the Hill coefficient
256 and different drug sensitivity parameters, whereas the GR_{inf} and GR_{AOC} values showed minimal
257 correlation with other metrics. For complete *GR* curves and information on additionally tested
258 cell lines and drugs, see **Supplementary Fig. 3** and **Supplementary Table 1**.
259

260 Variability throughout the day depends on the drug and cell model

261 The presence of a robust circadian clock combined with drugs that efficiently affect growth in
262 a tumor model are promising prerequisites for identifying drug variability throughout the day.
263 However, these prerequisites do not provide a priori insights into the specific time-of-day
264 response profile. To systematically screen ToD drug sensitivities, we developed a new
265 experimental strategy designed to significantly reduce the investigator's workload and number
266 of consecutive drug perturbations, thereby increasing throughputness, reproducibility and
267 accuracy (**Fig. 4a**). In this new approach, cell populations are seeded 24 h prior to the start of
268 continuous live-cell imaging followed by performing a 3-step circadian clock resetting protocol
269 in which separate cell populations receive a dexamethasone pulse at three different times (0, 4,
270 8 h). To test cells in later stages of the circadian cycle, drugs are administered at their estimated
271 half effective dose 32 and 48 h after the first resetting step, creating a range of time differences
272 between reset and treatment of 0, 4, 8, 16, 20 and 24 h in relative circadian time (**Fig. 4a**, *right*
273 *panel*). The effects of the different treatment times on cell growth were monitored by live-cell
274 imaging up to day 6, enabling the evaluation of drug responses for 4 days in both treatment
275 groups, as shown for the alisertib-treated TNBC cell line HCC1937 in **Fig. 4b**. In typical ToD
276 assays, cells are constantly proliferating during the 24 hours of ToD treatments, resulting in
277 varying cellular densities at the time of the drug treatments. These varying cell densities have
278 the potential to influence drug responses in vitro, possibly concealing or introducing bias when
279 determining ToD-specific drug effects. To account for different cell densities at the time of

280 treatment, drug responses are determined as the ratio of the number of cells at the time of each
281 treatment to the number of cells 96 h after each treatment, keeping the time-window from
282 treatment to evaluation identical across conditions (**Fig. 4c**, *left panel*). To highlight relative
283 response differences within a day, results are presented relative to the circadian time of 0 h.
284 Values >1 indicate increased resistance, while values <1 indicate higher sensitivity compared
285 to treatment at time 0 h (**Fig. 4c**, *right panel*). We quantify the maximum variability in relative
286 responses as the ToD Maximum Range (ToD_{MR}).
287 Our next objective was to explore the variability of ToD profiles of different drugs within a
288 subset of TNBC cells. To accomplish this, we screened ten cell line models shown in **Fig. 3**
289 treated with eight different drugs, generating approximately 80 ToD profiles (**Fig. 4d,e** and
290 **Supplementary Fig. 4a,b**). Comparing examples from individual cell lines, namely HCC1937
291 and MCF10A, revealed that HCC1937 exhibited relatively conserved ToD profiles, whereas
292 the non-malignant cell line showed greater ToD variability for the different drugs (**Fig. 4d**).
293 Furthermore, ToD sensitivity profiles varied significantly from drug to drug (**Fig. 4e** and
294 **Supplementary Fig. 4b**), suggesting that ToD profiles may be highly dependent on the cancer
295 cell model and drug mechanism of action.
296 To assess varying time-of-day sensitivities across all tested cell line models and drugs, we
297 calculated the corresponding ToD_{MR} value for each drug-cell combination (**Fig. 4f**). Averaging
298 the ToD_{MR} values per drug and cell line revealed a gradual ranking of ToD variability for each
299 drug and cell model tested (**Fig. 4g**). Within the drug panel, the highest and lowest ToD
300 variability was observed for cisplatin and alisertib, respectively, with a ~2-fold difference in
301 the average ToD_{MR} value (**Fig. 4g,** *top panel*). Similarly, the ToD variability of the tested cell
302 lines varied by ~2-fold, with MCF10A showing the highest and HCC38 the lowest average
303 variability. Considering only cancer cell lines, SUM149PT ranked highest and showed a
304 similar degree of ToD sensitivity variability as the non-malignant cell line (**Fig. 4g**, *bottom*
305 *panel*).
306 To assess the impact of circadian clock disruptions on ToD-dependent drug sensitivity, we
307 evaluated circadian-perturbed U-2 OS *Cry1/2*-dKO cells, alongside wild-type cells that
308 demonstrated the strongest circadian rhythms in our assessments (see **Fig. 2**). Using our ToD
309 treatment approach (see **Fig. 4a**), we tested three drugs which elicited high ToD response
310 variations in our breast cancer panel (see **Fig. 4g**), and which target distinct molecular
311 pathways. Our results demonstrate substantial ToD-dependent drug sensitivity in WT cells and

312 markedly reduced responses in *Cry1/2*-dKO cells (**Supplementary Fig. 4c**). Specifically,
313 ToD_{MR} values decreased by 62% for cisplatin, 58% for paclitaxel, and 40% for 5-FU in *Cry1/2*-
314 dKO compared to WT cells (**Supplementary Fig. 4d**), highlighting a critical role of the
315 circadian clock in influencing drug sensitivity throughout the day.
316 Together, our findings reveal distinct ToD profiles across most tested drugs and models,
317 highlighting individualized ToD sensitivity within distinct drugs and cell models despite the
318 common TNBC categorization and shared drug-target pathways.
319

320 Determining treatment times for maximum drug effect

321 The critical factor in the design of future chronotherapeutic treatments may be not only be the
322 sensitivity of cancer cells, but rather the differential time-of-day sensitivity between cancer and
323 non-malignant tissues[26]. To illustrate this, we compared the ToD response profiles of TNBC
324 cancer cell models with the profile of MCF10A, as shown for HCC1937 and alisertib in **Fig.**
325 **4h**. In this case, the cancer and non-malignant cell models show an antiphasic ToD response
326 profile, with an almost inverted profile. By calculating the greatest response differences
327 between the two cell models, we determined the treatment times of maximum and minimum
328 benefit (**Fig. 4h–j**). Analyzing the entire panel of tested drugs per cell line model and plotting
329 polar density histograms of the times of maximum and minimum benefit, we found that highest
330 overall benefit is achieved at 10–12 h and 18–20 h in the treatment of HCC1937, while earlier
331 treatment times of the day yield minimum benefit. In contrast, SUM149PT and MDAMB231
332 show a single prominent time window throughout the day that provides maximum treatment
333 benefit (**Fig. 4i**). In addition to cell model-to-model variability in the benefit times, we explored
334 the drug-to-drug variability by calculating the polar density histogram for the individual drugs
335 tested across all cell line models (**Fig. 4j**). 5-FU showed a clear preference for administration
336 between 8 and 10 h, while torin2 and paclitaxel showed more variability in maximum and
337 minimum benefit times, indicating different response relationships to the non-malignant cell
338 model across the cancer cell lines tested.
339 Finally, we quantified the extent of maximum and minimum treatment benefit by calculating
340 the corresponding fold changes in ToD responses between the cancer and non-malignant cell
341 model (**Fig. 4k**). By averaging these fold changes across cell lines and drugs, we established a
342 ranking referred to here as the "chronotherapeutic index". While the average ToD variability

343 highlights the benefits of a single model (**Fig. 4g**), the chronotherapeutic index reveals
344 distinctions between the cancer models and the non-malignant MCF10A cell model, thereby it
345 is offering valuable insights into the potential advantages of adopting a chronotherapeutic-
346 based schedule. It's worth noting that the rankings based solely on average ToD variability
347 within a single model or drug didn't align completely with the ranking of the chronotherapeutic
348 index. This emphasizes the importance of evaluating effects in relation to healthy tissues when
349 considering chronotherapy applications (**Fig. 4g,k**).
350 To sum up, our findings emphasize distinct chronotherapeutic response dynamics in vitro
351 between cancer and healthy cell models, underscoring two key objectives of chronotherapy:
352 pinpointing optimal treatment times to maximize cancer toxicity while minimizing impacts on
353 healthy tissues.
354

355 The relationship between time-of-day profiles and clock, growth, and drug 356 sensitivity metrics

357 The time-of-day sensitivity in cancer models results from complex interactions involving the
358 circadian clock, cancer cell growth, and drug responses. However, the specific mechanisms
359 governing these interactions remain largely unknown. To address this, we employ statistical
360 tools, including linear regression, dominance analysis, and determinant ranking, to uncover the
361 main parameters influencing a key aspect of ToD sensitivity curves, namely the maximum
362 range in responses (ToD_{MR}) (**Fig. 5a**). To explore how individual metrics relate to ToD_{MR}
363 values, we first performed pairwise linear regression analysis (**Fig. 5b–f**). We considered each
364 circadian channel individually or combined and found the strongest and most significant
365 correlations for clock metrics from the *Bmal1* channel (**Fig. 5d** and **Supplementary Fig. 5a,**
366 see **Supplementary Table 2** for a complete set of circadian metrics across the cell models
367 tested). ToD_{MR} values of 5-FU were significantly correlated with amplitudes (r=0.8, R^2=0.6)
368 and the prominence of circadian component (circadianicity) of the *Bmal1* signal (r=0.7,
369 R^2=0.43), whereas other circadian clock metrics were poorly associated (**Fig. 5b**,**d**). On the
370 other hand, we observed no significant and rather low associations for ToD_{MR} values and
371 growth metrics as well as for ToD_{MR} values and drug sensitivity metrics (**Fig. 5c,e,f**). To
372 identify the best associated individual metric and drug, we integrated all correlations and
373 generated a ranking as shown in **Fig. 5g**. For the different metrics, we observed the highest

correlation for the amplitude (r=0.43±0.02, mean±s.e.m.). Among the individual drugs, adavosertib ranked highest in overall correlation (r=0.39±0.03, mean ± s.e.m.) between ToD_{MR} values and the different metrics. Relative average associations between all metrics and ToD_{MR} values were predominantly positive, with only five metrics demonstrating inverse relationships (**Supplementary Fig. 5b**). Notably, only one drug, paclitaxel, displayed average negative associations across all metrics. To further test the associations between individual cellular parameters and ToD_{MR} values, we applied a linear regression model and compared calculated versus actual ToD_{MR} values of up to five new cell line models in Bland-Altman plots (**Supplementary Fig. 5c**, see **Supplementary Table 3** for the complete new dataset). This revealed mean biases of -0.04, -0.05, and 0.06 between calculated and actual ToD_{MR} values for the clock, growth, and drug sensitivity metrics, respectively. As also shown in **Supplementary Fig. 5c**, mean biases are near zero and most predicted data points lie within the limits of agreement, which indicates minimal overall bias and good agreement between the predicted and observed data points.

While linear regression approaches are robust for examining individual metrics, they do not provide relative information about which metrics have the most significant impact on ToD_{MR} values. To address this, we used dominance analysis and systematically tested all possible combinations of metrics. By measuring how much each metric improved the accuracy of the model when added or removed, we identified the highest contributing ones to the ToD_{MR} values of the different drugs. For alpelisib our analysis identified the amplitude of *Bmal1* signals as most important factor, accounting for 42% of the observed ToD sensitivity variability (**Fig. 5h**). In contrast, paclitaxel and adavosertib showed the most homogeneous distribution of individual contributions, with no single metric appearing especially important. Considering the shares of each determinant combined for all drugs led to a ranking of determinants as shown in **Fig. 5i**. Here, we observed the largest contributions for the *Bmal1* amplitude (mean = 21.9%) and smallest for the Hill coefficient of drug response curves (mean = 9.9%).

In summary, we were able to identify systematic dependencies of the maximal time-of-day drug sensitivities and different circadian clock, growth and drug sensitivity parameters. We have further shown that the relative importance of the different determinants varies substantially depending on the specific drug, highlighting the importance of considering multiple factors in understanding the time-of-day dependent variability of drug response in a cell model.

406

407 **Differential impact of core clock genes in shaping time-of-day sensitivity of**
408 **cancer models**

409 Beyond a cancer model's circadian clock, growth, and drug features, the expression levels of
410 core circadian clock genes are likely to contribute to the time-of-day sensitivity profiles. Thus,
411 we explored the connection between the expression patterns of 16 essential clock genes and
412 the maximum range in ToD sensitivity profiles (ToD_{MR}). We defined core clock genes as those
413 that directly control the transcriptional-translational feedback loops of the molecular clock
414 network and whose dysregulation or mutations result in disrupted circadian rhythms[31,32]. The
415 selected gene panel displayed distinct expression patterns across the TNBC cell lines tested
416 (**Supplementary Fig. 6a**). To examine potential relationships between core clock genes and
417 ToD_{MR} values, we used three different methods, namely linear correlation analysis,
418 dimensionality reduction by linear discriminant analysis (LDA) and principal component
419 analysis (PCA) (**Fig. 6a**).
420 Linear correlation analysis revealed significant correlations between ToD_{MR} values of five
421 tested compounds from our drug panel and selected core clock genes (**Fig. 6b**). Focusing on
422 the mitosis inhibitor paclitaxel, we identified particularly strong anticorrelations with the
423 expression levels of *Per3* (r=-0.88, R^2=0.78) and *Dbp* (r=-0.72, R^2=0.51) (**Fig. 6b,c**). Yet,
424 overall correlation between circadian clock genes and ToD_{MR} values were relatively weak,
425 which got also apparent when accumulating absolute correlations per drug or per metric
426 (**Supplementary Fig. 6b)**. Here, highest overall correlation of ToD_{MR} values were found for
427 cisplatin (r=0.40±0.21, mean±s.d.), while *Per2* was most associated with ToD_{MR} values among
428 the circadian clock gene panel (r=0.48±0.20, mean ± s.d.) (**Supplementary Fig. 6b**).
429 To assess the cumulative impact of circadian gene expression on the strength of time-of-day
430 effects as indicated by the ToD_{MR} values, aiming to uncover more complex patterns that might
431 not be explainable through linear correlations alone, we proceeded to apply LDA on a drug-
432 by-drug basis. To do so, we first categorized cell models into two groups based on the median
433 ToD_{MR} value for each drug. **Fig. 6d** provides an example using paclitaxel, effectively
434 separating the data into groups of high and low ToD_{MR} values. Implementing LDA to examine
435 the individual linear discriminant components of each circadian clock gene revealed a clear
436 ranking of genes in terms of their importance in discriminating the cell lines into the two ToD_{MR}

437 groups. For paclitaxel, the core clock genes *Cry2*, *Dbp*, and *Per3* were the most important
438 contributors to the specific discrimination, collectively accounting for approximately 46% of
439 the discriminative information (**Fig. 6d**, *right panel*). Importantly, the contribution of each gene
440 in discriminating between ToD_{MR} response groups varied for the tested drugs, suggesting that
441 either the drug or the drug targets may interact differently with the molecular components of
442 the circadian clock (**Supplementary Fig. 6c–i**). To explore the circadian clock's impact on
443 ToD sensitivity across various drug treatments, we assessed the overall contribution of each
444 gene by cumulating their effects across all drugs. This revealed modest overall contributions,
445 with the highest ranking *Rorβ* accounting for 10.5%±9.6% (mean±s.d.) of the discriminative
446 information (**Fig. 6e**).
447 While LDA is a powerful method to determine the discriminatory contribution of the individual
448 core clock genes, PCA allows for identifying underlying patterns and relationships among the
449 different genes. For paclitaxel, PCA distributed the cell models well along the first two
450 principal components which combined explained 73.7% of the variability among the different
451 ToD sensitivity profiles (**Supplementary Fig. 6j**, *left panel*). Ranking of the PC loadings
452 showed that the degree of contribution of each circadian clock gene in shaping the PCA
453 outcome was highly individual. For paclitaxel, *Csnk1d* was the major contributor to the ToD
454 sensitivity variability within the first principal component, while along the second principal
455 component, *Clock* ranked as main contributor (**Supplementary Fig. 6j**, *right panels*).
456 Collectively, our findings suggest limited associations between individual expression levels of
457 core clock genes and the observed ToD maximum ranges within the examined cell lines.
458 However, we found interesting relationships when considering the circadian clock gene panel
459 as a collective, indicating potential connections between the molecular circadian clock and
460 drug-dependent time-of-day sensitivity.
461

462 ## Discussion

463 While the fundamental role of the circadian clock in influencing disease progression and
464 treatment response is widely recognized[22,33,34], our understanding of the underlying biological
465 mechanisms remains fragmented. Approaches that enable the precise study of drug-
466 perturbations and treatment responses within controlled circadian-timed environments play a
467 pivotal role in advancing our understanding of the effects regulated by the circadian clock. To

468 date, there has been a notable absence of standardized methodologies for the comprehensive
469 exploration of the chronotherapeutic potential of drugs and cancer models. In this work we
470 present an integrative approach for the high-throughput quantification of time-of-day response
471 profiles and the elucidation of circadian, growth and drug sensitivity factors that shape these
472 profiles (**Fig. 1**). This innovative method holds significant promise for advancing biological
473 discovery, offering a robust platform to explore the intricate interplay between circadian
474 rhythms, cellular growth, and drug timing efficacy.
475 Despite the general expectation that the circadian clock is likely dysregulated in highly
476 transformed cancers[19,33], our approach reveals robust rhythms in numerous cancer cell models,
477 whose circadian properties were previously unknown (**Fig. 2**). Furthermore, our assessment of
478 circadian rhythms in non-malignant epithelial cells, luminal breast cancer cells, and
479 osteosarcoma cells aligns with prior research[28,35-37], underscoring the versatility of our
480 approach in elucidating circadian clock properties across various cancer and tissue types.
481 Among these, we focused on triple-negative breast cancer, a highly aggressive and
482 heterogeneous subtype, representing about 15% of diagnosed breast tumors. Current therapies
483 are ineffective, with cytotoxic chemotherapy still being an integral part of treatment despite
484 limited efficacy and severe side effects[38]. Our investigation into the growth dynamics and drug
485 responses of multiple TNBC cell models has generated a diverse array of metrics. Notably, our
486 results indicate that our set of drug sensitivity metrics, namely the GR_{50}, GEC_{50}, GR_{AOC}, GR_{inf}
487 and the Hill coefficient, exhibit milder correlations to each other, which is in agreement with
488 recent studies[39]. This challenges the conventional binary classification of sensitive versus
489 resistant models and suggests that drug sensitivity rankings are rather drug-dependent and
490 sensitivity metric-specific (**Fig. 3**).
491 By implementing our screening approach for the profiling of drug sensitivities across different
492 times of the day, we generated approximately 80 distinct time-of-day sensitivity profiles,
493 unveiling a wide range of sensitivity variations across drugs and cell line models (**Fig. 4** and
494 **Supplementary Fig. 4**). We then ranked models by their time-of-day sensitivity and observed
495 up to 30% response differences throughout the day for the top scoring models. We further
496 detected substantial variation in time-of-day sensitivity among the panel of drugs tested,
497 revealing previously unknown time-of-day dependent drug effects. Consistent with previous
498 findings, we show time-of-day dependent variability in responses to the DNA synthesis
499 inhibitors 5-FU[22,23,40] and doxorubicin[22,41] as well as to the DNA intercalator cisplatin[22,41].

500 Furthermore, we have introduced a novel chronotherapeutic index, which gauges the relative
501 advantages of adopting a circadian-based drug schedule. Various non-malignant cell models
502 may be employed for calculating this index, tailored to the particular disease model under
503 investigation. For example, fibroblast models, whose strong circadian rhythms have been
504 described in several works[42-44], are expected to show unique relationships with cancer models
505 in terms of sensitivity patterns at different times of the day.
506 Delving into the molecular mechanisms that potentially govern time-of-day sensitivity, our
507 novel method has unraveled key relationships between circadian clock dynamics, growth
508 patterns, and drug sensitivities, all of which significantly impacting time-of-day drug
509 responses. It is noteworthy that the specific contribution of these parameters varies depending
510 on the drug under consideration, underscoring the multifactorial nature of time-of-day
511 dependent variability in drug reactions (**Fig. 5**). Aiming to simplify the circadian analysis and
512 to provide an overarching view on circadian clock dynamics, we initially combined *Bmal1*-
513 and *Per2*-signals in Fig. 2. However, separate evaluations of the circadian genes, as presented
514 in **Supplementary Fig. 1e and f**, proved crucial to elucidate the significant impact of
515 oscillatory *Bmal1* dynamics on ToD_{MR} values.
516 In an exploratory approach, we identified limited associations between expression levels of
517 core circadian clock genes and ToD sensitivities (**Fig. 6**). This may hint to a more complex role
518 of the molecular circadian clock network in this context, where distinct associations might be
519 masked by high redundancy and interconnection between core clock genes. Additionally, our
520 results could indicate a discrete role of the cell cycle in shaping our observed ToD sensitivity
521 profiles[45-47], which also invites for further research in that context.
522 Assessing the cumulative impact of circadian gene expression on ToD_{MR} values, we found
523 differential contributions of each circadian gene in discriminating between high and low ToD-
524 dependent sensitivity based on the drug tested. To investigate whether this observation
525 underlies variations in the expression levels of the drug targets, follow-up explorations
526 involving e.g. mRNA or protein quantification techniques performed at different times of the
527 day could be conducted in future studies focusing on the molecular mechanisms of ToD
528 sensitivity.
529 Given their recognized influence on pharmacodynamics[22,33,34], our study primarily focused on
530 circadian rhythms. Nevertheless, our multiresolution analysis of *Bmal1* and *Per2* oscillatory
531 signals uncovered distinct alternate rhythms of shorter and longer periods, as illustrated in **Fig.**

532 **2i** and **j**. The significant impact of independent 12-hour ultradian rhythms on stress responses
533 has been previously documented for mammalian cells[48], and constitutes an interesting field for
534 future research in the scope of our time-of-day drug sensitivity profiles.
535 Despite employing a robust method to introduce luciferase reporters and validating several
536 circadian results, as well as using population-based recordings of non-clonal cell lines, our
537 approach does not rule out the potential impact of random reporter insertions on circadian clock
538 estimation. Moreover, while our findings are primarily based on in vitro models and are not
539 directly applicable for treatment recommendations, our framework can be directly applied to
540 model organisms of higher complexity, such as 3D patient-derived organoids and animal
541 models where the circadian clock can be tracked.
542 Altogether, we provide a comprehensive method to determine optimal drug treatment times of
543 complex diseases and to identify the cell subtypes that will most benefit from a time-of-day
544 based treatment. Leveraging innovative experimental and computational techniques our
545 approach further elucidates the specific biological features that shape time-of-day response
546 profiles, thereby advancing our understanding of the cellular mechanisms that drive time-of-
547 day sensitivity. As a result, our method provides tools to uncover the cellular mechanisms that
548 govern time-of-day sensitivity, paving the way for new biological discoveries.
549

550 ## Acknowledgements

551 We thank Malthe Skytte Nordentoft Nielsen as well as the laboratories of Michela Di Virgilio
552 and Ingeborg Tinhofer-Keilholz for their valuable feedback to our project. We would like to
553 express our gratitude to Annika Winkler and Marie Möser for their assistance with sample
554 preparation, as well as to Sofía Peso-García and Franziska Reiher for their experimental
555 support. We further thank Christian Gabriel and Valentina Alejandra Balde Araya for valuable
556 feedback during the review of this manuscript. Lastly, we sincerely thank the editor and
557 anonymous reviewers for their comprehensive review of our manuscript and for providing
558 constructive feedback which allowed us to significantly improve our manuscript. The results
559 are part of a project funded by the German Federal Ministry of Education and Research
560 (BMBF) through the e:Med Juniorverbund DeepLTNBC TP3-01ZX1917C. C.E. was partially
561 supported by the Deutsche Forschungsgemeinschaft (DFG, German Research Foundation)–
562 RTG2424/CompCancer – project number: 377984878 and is enrolled in the doctoral program

563 of the Berlin School of Integrative Oncology (BSIO). C.S. acknowledges support from the
564 DFG–SCHM 3362/4–1 project number: 511886499.
565

566 # Materials and Methods

567 ## Experimental methods

568 ### Cell culture

569 HCC1143, HCC1806, HCC1937, HCC38, and MDAMB468 cells were obtained from the
570 American Type Culture Collection. BT549, CAL51, MDAMB231, MDAMB436 and
571 SUM149PT cells were kindly provided by the Sorger lab (Harvard Medical School, Ludwig
572 Cancer Center, Boston, USA). MCF10A and MCF7 cells were kindly gifted by the Brugge lab
573 (Harvard Medical School, Ludwig Cancer Center, Boston, USA). GIMEN and SH-SY5Y cells
574 were provided by the Schulte lab (Universitätsklinikum Tübingen, Clinic for Pediatrics and
575 Adolescent Medicine, Thübingen, Germany) and the U-2 OS reporter cell lines by the Kramer
576 lab (Charité, Institute for Medical Immunology, Berlin, Germany). MCF10A cells were
577 maintained according to the Brugge lab's media recipe based on DMEM/F12 media (Gibco)
578 supplemented with 5% horse serum (Gibco), 20 ng/ml EGF (Peprotech), 0.5 mg/ml
579 Hydrocortisone (Sigma), 100 ng/ml Cholera Toxin (Sigma), 10 µg/ml Insulin (Sigma) and 1%
580 penicillin-streptomycin (Pen-Strep, Gibco). All other cell lines were maintained in RPMI 1640
581 (Gibco) supplemented with 10% fetal bovine serum (FBS) (Gibco) and 1% Pen-Strep. For
582 bioluminescence recordings and long-term imaging, cells were cultured in FluoroBrite DMEM
583 medium (Gibco) supplemented with 10% FBS, 300 mg L-Glutamine (Gibco) and 1% Pen-
584 Strep. Cells were kept at 37 °C in a humidified 5% CO_2 environment and regularly tested for
585 mycoplasma.

586 ### Generation of reporter cell lines

587 To produce lentivirus carrying constitutive red-fluorescent nuclear reporters, HEK293T cells
588 at 80% confluence were transfected with a mix of 1.8 µg gag/pol packaging plasmid (Addgene
589 #14887), 0.7 µg pRev packaging plasmid (Addgene #12253), 0.3 µg VSV-G envelope plasmid
590 (Addgene #14888) and 3.2 µg of a plasmid with a EF1α-mKate2-NLS sequence. Lentivirus

591 expressing either *Bmal1*- or *Per2*-promoter driven luciferase reporter was produced by
592 transfecting HEK293T cells with 6 µg psPAX2 (Addgene #12260), 3.6 µg pMD2G (Addgene
593 #12259) and 8.4 µg lentiviral expression plasmid (pAB-mBmal1:Luc-Puro or plenti6-
594 mPer2:Luc-Blast, respectively). Transfections were conducted using Lipofectamine 3000
595 (Invitrogen) according to the manufacturer's instructions and media was replaced by RMPI
596 1640 medium supplemented with 10 mM HEPES before adding the transfection mixture.
597 Lentiviral supernatant was collected after 48 h and 72 h and passed through a 0.45 µm filter
598 (Millipore). For lentiviral transduction, receiver cells at 70% confluence were incubated with
599 a mix of 1 ml lentivirus-containing supernatant, 8 µg/ml protamine sulfate (Sigma) and 10 µM
600 HEPES (Gibco) for 6 h. Ensuing, cells were washed with PBS (Gibco) and cultured in their
601 regular culture medium for 2 days before starting antibiotic selection of transduced cells. To
602 select for transduced cells, cells were grown in medium containing 5 µg/ml blasticidin (Adooq)
603 or 2 µg/ml puromycin (Gibco) according to the resistance cassette on the lentiviral expression
604 plasmid until non-transduced control cells died. Details about the generation of the U-2 OS
605 *Cry1*-sKO, U-2 OS *Cry2*-sKO, and U-2 OS *Cry1*/*Cry2*-dKO cell lines can be found in the
606 original publication by Börding *et al.*[28].

607 Bioluminescence recordings

608 Cells expressing *Bmal1*- or *Per2*-promoter driven luciferase reporters were seeded in 35-mm
609 dishes (Nunc) to reach approximate confluence on the following day. To account for potentially
610 different phases of single-cell circadian clocks in cell populations, we collectively reset the
611 circadian clocks by administering a standard dose of 1 µM dexamethasone[49,50] (Sigma,
612 dissolved in EtOH). After 30 min incubation cells were washed once with PBS and imaging
613 medium supplemented with 250 µM D-Luciferin (Abmole) was added. To avoid evaporation
614 of the media throughout the bioluminescence recordings, the dishes were sealed with parafilm
615 as described in Finger *et al.*[49]. Luminescence intensity was monitored at 10-min intervals for 5
616 days in an incubator-embedded luminometer (LumiCycle, Actimetrics). Bioluminescence
617 recordings were conducted using two biological replicates. For each individual experiment,
618 three, in some cases only two, technical replicates were assessed. MCF10A cells have been
619 tested on a single day using three technical replicates.

620 ## Long-term live-cell imaging

621 All live-cell imaging experiments were performed with cells expressing the fluorescent
622 mKate2-NLS nuclear reporter, seeded in 48-well plates (Falcon) at a density that saturates at
623 unperturbed growth conditions towards the end of each experiment. Long-term live-cell
624 imaging was conducted using an incubator-embedded Incucyte live-cell widefield microscope
625 (Essen BioScience). Cells were imaged in the brightfield and for nuclei segmentation and cell
626 counting in the red channel (excitation: 567–607 nm, emission: 622–704 nm). Images were
627 analyzed by frame-by-frame nuclei counting with the in-built Incucyte software and results
628 were further processed in MATLAB. For experiments that involved drug treatments, cells were
629 seeded 1 day before starting the live recordings and images were taken using a 4x magnification
630 lens in 2 fields-of-views per well every 1–2 h for a total duration of 4–6 days. Two independent
631 plates per condition were assayed in a single experiment. For drug response experiments with
632 cisplatin a single plate per condition was assayed in a single experiment, imaged in 9 fields-of-
633 views per well using a 10x magnification lens. For experiments capturing unperturbed growth
634 dynamics, 300–1000 cells, corresponding to ~10% confluency, were seeded 2 days before
635 starting the live recordings. Using a 10x magnification lens, 9 images per well were acquired
636 in 1–2 h intervals for a total duration of 4 days.

637 ## Dose-response curves

638 Drug stock solutions (100–10 mM) were prepared in DMSO and preserved at -20°C. Cisplatin
639 (Sigma) stock solution of 3.33 mM was prepared in 0.9% NaCl and stored at room temperature.
640 For dose-response assays, a serial 5–6 point log4 dilution of each drug was freshly prepared in
641 its solvent prior to treatment. Following concentration ranges were tested: 100–0.1 μM for 5-
642 fluorouracil (5-FU, Sigma), alpelisib (Biozol) and olaparib (Adooq); 10–0.01 μM for torin2
643 (Sigma) and alisertib (Hölzel); 10–0.04 μM for adavosertib (Biocat); 1–0.004 μM for
644 doxorubicin (Hölzel); and 0.4–0.0004 μM for paclitaxel (Hölzel). Cisplatin was tested in a
645 serial 10-point log2 dilution with doses ranging from 70–0.14 μM. Compounds were added to
646 the cells one day after cell seeding in a drug-media mixture of 9% of total well-volume.
647 Solvent-only treated control cells were assayed along the treated conditions. Each tested
648 condition contained equal amounts of the solvent. Cell growth was monitored by live-cell
649 imaging for at least 4 days as described above.

650 ## Time-of-day treatments

651 Cells were seeded and allowed to attach overnight. The next day, live recordings commenced
652 as described earlier. We performed independent resetting steps every 4 h over an 8-h period,
653 creating distinct cell populations at 0, 4, or 8 h of circadian time. Subsequently, we
654 administered the same drug concentration, which corresponded to the estimated half-maximal
655 effective concentration, at either 32 or 48 h after the initial resetting step. This allowed us to
656 simultaneously test six different circadian stages (0, 4, 8, 16, 20, and 24 h). Drug concentrations
657 were determined separately for each cell line and drug combination. For cisplatin, the
658 treatments we performed slightly different, using 4 independent resetting steps every 3 hours
659 over a 9-h period followed by drug treatments 32 or 48 h post initial resetting. In all cases, cell
660 growth was continuously monitored through long-term live-cell imaging for a total of 6 days.

661 ## Computational methods

662 ## Time-series analysis of circadian signals

663 **Detrending.** Raw time-series data were detrended by applying a sinc filter with a 48-h cut-off
664 period using the open-source software package pyBOAT[27] (v0.9.1) within the Anaconda
665 Navigator (v1.10.0).
666 **Amplitude envelope and normalization**. Continuous amplitude envelope calculation was
667 obtained using continuous wavelet transform implemented in pyBOAT with a time window of
668 48 hours. The amplitude normalization was done by taking the inverse of the envelope of the
669 detrended signal as described in Mönke G*, et al.* [27] .
670 **Autocorrelation analysis.** Periodicity data was assessed by calculating its autocorrelation and
671 abcissa at the second peak using the 'autocorr' and 'findpeaks' MATLAB functions[51] from the
672 detrended time-series.
673 **Continuous wavelet transform.** The main oscillatory component, known as the ridge
674 component, was obtained using a wavelet-based spectral analysis from amplitude-normalized
675 and detrended signals. For the ridge detection we used both an adaptable-threshold and a fixed-
676 threshold. The adaptable threshold was based on each signal's half-maximal spectral power
677 and was implemented for the "period" and "phase difference" metric shown in Fig. 2 and Fig.
678 S1. The instantaneous phase difference between the *Bmal1* and *Per2* signals was calculated
679 using the MATLAB 'atan2' function (Supplementary Fig. 1a) and for the polar histogram

representation, we deployed the 'polarhistogram' function and the 'Circular Statistics Toolbox' (v1.21.9.0. by Philipp Behrens) from MATLAB (Supplementary Fig. 1b). For the analysis of "amplitudes" and "ridge lengths" shown in Fig. 2 and the determinants for time-of-day sensitivity shown in Fig. 5, the metrics of the main oscillatory component were derived using a fixed-ridge threshold of 40. This ridge threshold value was chosen as it offered a well-balanced threshold suitable for comparing signals of varying strengths.

Multiresolution analysis. Detrended time-series data were decomposed into a set of different wavelet details D_j representing distinct disjoint frequency bands and a final smooth using a discrete wavelet transform based multiresolution analysis[52]. The algorithm has been implemented using the 'PyWavelets' python package[53], with a *db20* wavelet of the Daubechies wavelet family as previously described in Myung, Schmal and Hong *et al.*[54]. Since each wavelet detail D_j represents a period range between $2^j\Delta t$ and $2^{j+1}\Delta t$ (for j=1, 2, 3, …) we down-sampled the time series from a Δt=10 min to a Δt=30 min sampling frequency to obtain a circadian period band between 16–32 h for further analysis. Since the MRA decomposes the variance of the detrended signal with respect to the different disjoint period bands it can be used to determine the rhythmicity of the signal in the circadian period range[55].

Global circadian strength. To calculate the global circadian strength (*GCS*) of a cell line model *i*, the autocorrelation peak value (peak), the wavelet-based continuous ridge length (ridge) and the discrete circadianicity component (circadianicity) were normalized to the respective maximum (max) value measured among all tested cell line models and averaged according to the following equation:

$$GCS_i = \text{mean}\left(\frac{\text{peak}_i}{\text{peak}_{\text{max}}}, \frac{\text{ridge}_i}{\text{ridge}_{\text{max}}}, \frac{\text{circadianicity}_i}{\text{circadianicity}_{\text{max}}}\right)$$

Statistical analysis. Linear regression model fitting of *Bmal1* and *Per2* circadianicity components obtained by MRA was done with the 'fitlm' MATLAB function. Significant variances in circadian parameters between wild-type U-2 OS cells and both, *Cry1*-sKO and *Cry1/2*-dKO cells, were calculated with a one-way ANOVA and Tukey's post-hoc test using the 'anova1' and 'multcompare' MATLAB functions.

Multi-parametric analysis of growth dynamics

Growth data obtained from long-term live-cell imaging was smoothed using a robust local regression approach of weighted linear least squares and a 2nd degree polynomial model ('rloess' MATLAB function). Doubling times of smoothed cell numbers or confluency were calculated according to the following equation:

$$\text{Doubling time}(t) = t * \frac{\log(2)}{\log(y_0/y_t)}$$

where t refers to the time of assessment, in our case 96 h, and y_0 refers to the cell number at timepoint 0. To calculate the exponential growth rate k per unit of time t, we normalized cell numbers to the initial timepoint 0 (y_0) and fitted an exponential function to the growth curves:

$$\text{Growth}(t) = y_0 * e^{(k*t)}$$

Exponential function fitting was done with the MATLAB 'fit' function[51]. Linear regression model fitting to different combinations of growth parameters was done with the 'fitlm' MATLAB function.

Estimation of drug sensitivity parameters

Drug response data obtained from long-term live-cell imaging was smoothed using a robust local regression approach of weighted linear least squares and a 2nd degree polynomial model ('rloess' MATLAB function). Following the method established by Hafner *et al.*[30], we computed the growth rate inhibition (*GR*) at time *t* and for each dose *c* as follows:

$$GR(c,t) = 2^{k(c,t)/k(0)} - 1$$

where $k(c,t)$ is the growth rate under drug treatment and $k(0)$ is the growth rate of untreated cells. Drug response parameters were retrieved by fitting the dose-dependent *GR* values to a sigmoid curve using the following equation:

$$GR(c) = GR_{\text{inf}} + \frac{1 - GR_{\text{inf}}}{1 + (c/GEC_{50})^{h_{\text{GR}}}}$$

730 where the fitted parameters are as described in Hafner *et al.*[30]. Standard EC_{50} values were
731 calculated by fitting final nucleus counts, normalized to the respective count of the control, to
732 the following sigmoidal function:

733 $$f(c) = E_{\min} + \frac{1 - E_{\min}}{1 + (c/EC_{50})^{h}}$$

734 where $E_{\min}$ corresponds to the minimum response, restricted to values between 0 and 1, and h
735 is the hill slope of the response curve, constrained to 0.5–10. Sigmoidal function fitting steps
736 were done with the MATLAB functions 'fit' (*GR* metrics) or 'lsqnonlin' (EC_{50} value)[51].
737 Hierarchical clustering analysis was implemented with the MATLAB 'clustergram' function
738 using an euclidian distance and average linkage method[51]. To account for the different tested
739 dose ranges across drugs for clustering, GEC_{50} values were normalized to the dose at GR_{inf}.
740 Pearson's linear correlation coefficients across drug sensitivity metrics were computed using
741 the MATLAB 'corr' function. For the comparison of cellular growth dynamics to drug doses
742 evoking the maximum tested effect, we chose growth curves corresponding to the doses closest
743 to the determined GR_{inf} values.

744 Time-of-day sensitivity evaluation

745 Drug response data of time-of-day treatment experiments was smoothed using a moving
746 average ('smoothdata' MATLAB function). Final nucleus counts were normalized to the
747 nucleus count at the respective time of treatment. ToD response data from U-2 OS WT and
748 *Cry1/2*-dKO cell lines were obtained from confluency readouts in the brightfield channel.
749 Time-of-day response curves were generated from the relative final responses of each treatment
750 timepoint to the final response at timepoint 0 and interpolated using the 'smoothingspline'
751 function in MATLAB. The smoothing parameter was set to 0.7. The maximum range across
752 smoothed time-of-day responses (ToD_{MR}) was calculated by subtraction of the minimum from
753 the maximum relative response. To assess whether the smoothing of response data introduces
754 artifacts into ToD_{MR} estimates, we performed linear regression analysis between ToD_{MR} values
755 from raw and spline smoothed data using the 'fitlm' MATLAB function and confirmed a high
756 positive correlation (**Supplementary Fig. 7a**). ToD_{MR} values were clustered as described for
757 the drug sensitivity parameters, with missing data points substituted by values from the closest
758 relevant column, adhering to the 'nearest-neighbor' principle. Polar histograms of the treatment

759 times with maximum and minimum benefit were generated using the 'polarhistogram'
760 MATLAB function with 'probability' normalization to depict each bar's height as the fraction
761 of observations within its bin relative to the total observations.

762 Correlation and shapley value regression analysis

763 Linear regressions of cell-intrinsic features and drug-dependent ToD sensitivity have been
764 obtained using the 'stats' and 'optimize' modules of the 'SciPy' and the 'uncertainties' package
765 of the Python programming language. Predictions of ToD_{MR} values from new data was based
766 on fitting a linear regression model to the original data that was associated with Pearson
767 correlation coefficients ≥ 0.5, utilizing the 'fitlm' MATLAB function. Bland-Altman plots
768 comparing predicted and actual ToD_{MR} values were generated using the 'Bland-Altman and
769 Correlation Plot' package (v1.12.0.0) from MATLAB Central File Exchange (2017, Ran
770 Klein). Live-imaging data yielding growth, drug sensitivity, and ToD sensitivity metrics from
771 the new cell lines, utilized for the predictions, were based on the confluency readout due to
772 unviability of nuclear reporter cell lines for most models. Only the drug sensitivity metrics for
773 MCF7 were based on nuclear counts. The relative importance of the different parameters in a
774 multiple linear regression model are obtained by Shapley value regression via the Python
775 'dominance-analysis' package.

776 Circadian clock gene expression analysis

777 Gene expression data of circadian clock genes were obtained from the Cancer Cell Line
778 Encyclopedia Dependency Map (CCLE DepMap, https://sites.broadinstitute.org/ccle/datasets,
779 Q4 of 2022)[56]. Circadian clock genes of the individual breast cancer cell lines were clustered
780 using the 'clustermap' plotting function of 'seaborn' with the euclidian distance metric and
781 complete linkage method. Spearman rank correlation coefficients of circadian clock genes and
782 drug-specific ToD sensitivity values were computed using the spearman rank correlation
783 algorithm of the 'SciPy stats' python language module and hierarchically clustered with the
784 correlation distance metric and single linkage method. Regression plots were obtained using
785 the 'jointplot' plotting function from 'seaborn', showing drug-specific correlation between the
786 ToD sensitivities and gene expression of each cell line, including their distribution, squared
787 spearman rank correlation coefficient, *p*-value, and a confidence interval of 95%.

Supervised and unsupervised dimensionality reduction

Supervised dimensionality reduction by linear discriminant analysis was performed with the 'LinearDiscriminantAnalysis' function of the 'sklearn discriminant_analysis' python language module. The default parameters were retained, using the exact full singular value decomposition solver and 1 component. Median-based binarization of the drug-dependent ToD sensitivity values were used as target and the resulting linear discriminant vector was plotted using random y-axis units to avoid overlapping of the data points. The robustness of the discriminative information from the LDA was tested using a leave-one-out cross-validation (LOOCV) strategy (**Supplementary Figure 7b**). LOOCV was conducted using the 'model_selection' module from 'sklearn' in Python (v3.9.7) and implemented via the PyCharm Community Edition IDE (v2021.2.2). The contribution to the obtained discriminative information is shown in percentage for each of the circadian clock genes. Unsupervised dimensionality reduction by principal component analysis (PCA) was performed with the 'PCA' function of the 'sklearn decomposition' python language module using the exact full singular value decomposition solver and number of components equivalent to the sample size of the corresponding drug. Further analysis of the most informative PCA components was done by drawing the biplots of the first two principal components and showing the loadings of each circadian clock gene for both components.

Data availability

The experimental data and data tables for all results of this study are available in Figshare with the identifier https://figshare.com/projects/Time-of-Day-Drug-Response/180916.

Code availability

Code used for the data analysis in this work is available on GitHub: https://github.com/Granada-Lab/Time-of-Day-Drug-Response.

Competing interests

The authors declare no competing interests.

References

1 Chaix, A., Zarrinpar, A. & Panda, S. The circadian coordination of cell biology. *J Cell Biol* **215**, 15-25 (2016). https://doi.org/10.1083/jcb.201603076

2 Zhang, R., Lahens, N. F., Ballance, H. I., Hughes, M. E. & Hogenesch, J. B. A circadian gene expression atlas in mammals: implications for biology and medicine. *Proc Natl Acad Sci U S A* **111**, 16219-16224 (2014). https://doi.org/10.1073/pnas.1408886111

3 Mure, L. S. *et al.* Diurnal transcriptome atlas of a primate across major neural and peripheral tissues. *Science* **359** (2018). https://doi.org/10.1126/science.aao0318

4 Saini, C. *et al.* A functional circadian clock is required for proper insulin secretion by human pancreatic islet cells. *Diabetes, Obesity and Metabolism* **18**, 355-365 (2016). https://doi.org/doi.org/10.1111/dom.12616

5 Neufeld-Cohen, A. *et al.* Circadian control of oscillations in mitochondrial rate-limiting enzymes and nutrient utilization by PERIOD proteins. *Proc Natl Acad Sci U S A* **113**, E1673-1682 (2016). https://doi.org/10.1073/pnas.1519650113

6 Chakrabarti, S. & Michor, F. Circadian clock effects on cellular proliferation: Insights from theory and experiments. *Current Opinion in Cell Biology* **67**, 17-26 (2020). https://doi.org/https://doi.org/10.1016/j.ceb.2020.07.003

7 Scheiermann, C., Kunisaki, Y. & Frenette, P. S. Circadian control of the immune system. *Nature Reviews Immunology* **13**, 190-198 (2013). https://doi.org/10.1038/nri3386

8 Sancar, A. *et al.* Circadian clock control of the cellular response to DNA damage. *FEBS Lett* **584**, 2618-2625 (2010). https://doi.org/10.1016/j.febslet.2010.03.017

9 Schernhammer, E. S. *et al.* Rotating night shifts and risk of breast cancer in women participating in the nurses' health study. *J Natl Cancer Inst* **93**, 1563-1568 (2001). https://doi.org/10.1093/jnci/93.20.1563

10 Puram, Rishi V. *et al.* Core Circadian Clock Genes Regulate Leukemia Stem Cells in AML. *Cell* **165**, 303-316 (2016). https://doi.org/10.1016/j.cell.2016.03.015

11 Papagiannakopoulos, T. *et al.* Circadian Rhythm Disruption Promotes Lung Tumorigenesis. *Cell Metab* **24**, 324-331 (2016). https://doi.org/https://doi.org/10.1111/dom.12616

12 Chun, S. K. *et al.* Disruption of the circadian clock drives Apc loss of heterozygosity to accelerate colorectal cancer. *Science Advances* **8**, eabo2389 (2022). https://doi.org/doi:10.1126/sciadv.abo2389

13 Diamantopoulou, Z. *et al.* The metastatic spread of breast cancer accelerates during sleep. *Nature* **607**, 156-162 (2022). https://doi.org/10.1038/s41586-022-04875-y

14 Wang, J. *et al.* Circadian protein BMAL1 promotes breast cancer cell invasion and metastasis by up-regulating matrix metalloproteinase9 expression. *Cancer Cell International* **19**, 182 (2019). https://doi.org/10.1186/s12935-019-0902-2

15 Lee, Y. *et al.* G1/S cell cycle regulators mediate effects of circadian dysregulation on tumor growth and provide targets for timed anticancer treatment. *PLOS Biology* **17**, e3000228 (2019). https://doi.org/10.1371/journal.pbio.3000228

16 Chen, W.-D. *et al.* The circadian rhythm controls telomeres and telomerase activity. *Biochemical and Biophysical Research Communications* **451**, 408-414 (2014). https://doi.org/https://doi.org/10.1016/j.bbrc.2014.07.138

17 Rida, P., Syed, M. I. & Aneja, R. Time will tell: Circadian clock dysregulation in triple negative breast cancer. *Front Biosci (Schol Ed)* **11**, 178-192 (2019).

18 Innominato, P. F. *et al.* Prediction of overall survival through circadian rest-activity monitoring during chemotherapy for metastatic colorectal cancer. *International Journal of Cancer* **131**, 2684-2692 (2012). https://doi.org/https://doi.org/10.1002/ijc.27574

19 Ye, Y. *et al.* The Genomic Landscape and Pharmacogenomic Interactions of Clock Genes in Cancer Chronotherapy. *Cell Systems* **6**, 314-328.e312 (2018). https://doi.org/https://doi.org/10.1016/j.cels.2018.01.013

20 Lee, Y. *et al.* Time-of-day specificity of anticancer drugs may be mediated by circadian regulation of the cell cycle. *Science Advances* **7**, eabd2645 (2021). https://doi.org/10.1126/sciadv.abd2645

21 Dallmann, R., Brown, S. A. & Gachon, F. Chronopharmacology: New Insights and Therapeutic Implications. *Annual Review of Pharmacology and Toxicology* **54**, 339-361 (2014). https://doi.org/10.1146/annurev-pharmtox-011613-135923

874 22 Lévi, F., Okyar, A., Dulong, S., Innominato, P. F. & Clairambault, J. Circadian Timing in
875 Cancer Treatments. *Annual Review of Pharmacology and Toxicology* **50**, 377-421 (2010).
876 https://doi.org/10.1146/annurev.pharmtox.48.113006.094626

877 23 Wood, P. A., Du-Quiton, J., You, S. & Hrushesky, W. J. M. Circadian clock coordinates cancer
878 cell cycle progression, thymidylate synthase, and 5-fluorouracil therapeutic index. *Molecular*
879 *Cancer Therapeutics* **5**, 2023-2033 (2006). https://doi.org/10.1158/1535-7163.MCT-06-0177

880 24 Damato, A. R. *et al.* A randomized feasibility study evaluating temozolomide circadian
881 medicine in patients with glioma. *Neuro-Oncology Practice* **9**, 193-200 (2022).
882 https://doi.org/10.1093/nop/npac003

883 25 Ruben, M. D., Smith, D. F., FitzGerald, G. A. & Hogenesch, J. B. Dosing time matters. *Science*
884 **365**, 547-549 (2019). https://doi.org/doi:10.1126/science.aax7621

885 26 Kramer, A. *et al.* Foundations of circadian medicine. *PLOS Biology* **20**, e3001567 (2022).
886 https://doi.org/10.1371/journal.pbio.3001567

887 27 Mönke, G., Sorgenfrei, F. A., Schmal, C. & Granada, A. E. Optimal time frequency analysis
888 for biological data - pyBOAT. *bioRxiv*, 2020.2004.2029.067744 (2020).
889 https://doi.org/10.1101/2020.04.29.067744

890 28 Börding, T., Abdo, A. N., Maier, B., Gabriel, C. & Kramer, A. Generation of Human CRY1
891 and CRY2 Knockout Cells Using Duplex CRISPR/Cas9 Technology. *Front Physiol* **10**, 577
892 (2019). https://doi.org/10.3389/fphys.2019.00577

893 29 Leise, T. L. Analysis of Nonstationary Time Series for Biological Rhythms Research. *J Biol*
894 *Rhythms* **32**, 187-194 (2017). https://doi.org/10.1177/0748730417709105

895 30 Hafner, M., Niepel, M., Chung, M. & Sorger, P. K. Growth rate inhibition metrics correct for
896 confounders in measuring sensitivity to cancer drugs. *Nature Methods* **13**, 521-527 (2016).
897 https://doi.org/10.1038/nmeth.3853

898 31 Ko, C. H. & Takahashi, J. S. Molecular components of the mammalian circadian clock. *Hum*
899 *Mol Genet* **15 Spec No 2**, R271-277 (2006). https://doi.org/10.1093/hmg/ddl207

900 32 Takahashi, J. S. Transcriptional architecture of the mammalian circadian clock. *Nature Reviews*
901 *Genetics* **18**, 164-179 (2017). https://doi.org/10.1038/nrg.2016.150

902 33 Mormont, M.-C. & Levi, F. Cancer chronotherapy: Principles, applications, and perspectives.
903 *Cancer* **97**, 155-169 (2003). https://doi.org/https://doi.org/10.1002/cncr.11040

904 34 Sulli, G., Lam, M. T. Y. & Panda, S. Interplay between Circadian Clock and Cancer: New
905 Frontiers for Cancer Treatment. *Trends in Cancer* **5**, 475-494 (2019).
906 https://doi.org/https://doi.org/10.1016/j.trecan.2019.07.002

35 Lin, H.-H., Qraitem, M., Lian, Y., Taylor, S. R. & Farkas, M. E. Analyses of BMAL1 and PER2 Oscillations in a Model of Breast Cancer Progression Reveal Changes With Malignancy. *Integr Cancer Ther* **18**, 1534735419836494-1534735419836494 (2019). https://doi.org/10.1177/1534735419836494

36 Lellupitiyage Don, S. S. *et al.* Circadian oscillations persist in low malignancy breast cancer cells. *Cell Cycle* **18**, 2447-2453 (2019). https://doi.org/10.1080/15384101.2019.1648957

37 Baggs, J. E. *et al.* Network Features of the Mammalian Circadian Clock. *PLOS Biology* **7**, e1000052 (2009). https://doi.org/10.1371/journal.pbio.1000052

38 Gupta, G. K. *et al.* Perspectives on Triple-Negative Breast Cancer: Current Treatment Strategies, Unmet Needs, and Potential Targets for Future Therapies. *Cancers (Basel)* **12**, 2392 (2020). https://doi.org/10.3390/cancers12092392

39 Fallahi-Sichani, M., Honarnejad, S., Heiser, L. M., Gray, J. W. & Sorger, P. K. Metrics other than potency reveal systematic variation in responses to cancer drugs. *Nat Chem Biol* **9**, 708-714 (2013). https://doi.org/10.1038/nchembio.1337

40 Lévi, F. A. *et al.* Chronomodulated Versus Fixed-Infusion—Rate Delivery of Ambulatory Chemotherapy With Oxaliplatin, Fluorouracil, and Folinic Acid (Leucovorin) in Patients With Colorectal Cancer Metastases: a Randomized Multi-institutional Trial. *JNCI: Journal of the National Cancer Institute* **86**, 1608-1617 (1994). https://doi.org/10.1093/jnci/86.21.1608

41 Sothern, R. B., Lévi, F., Haus, E., Halberg, F. & Hrushesky, W. J. Control of a murine plasmacytoma with doxorubicin-cisplatin: dependence on circadian stage of treatment. *J Natl Cancer Inst* **81**, 135-145 (1989). https://doi.org/10.1093/jnci/81.2.135

42 Nagoshi, E. *et al.* Circadian gene expression in individual fibroblasts: cell-autonomous and self-sustained oscillators pass time to daughter cells. *Cell* **119**, 693-705 (2004). https://doi.org/10.1016/j.cell.2004.11.015

43 Izumo, M., Johnson, C. H. & Yamazaki, S. Circadian gene expression in mammalian fibroblasts revealed by real-time luminescence reporting: Temperature compensation and damping. *Proceedings of the National Academy of Sciences* **100**, 16089-16094 (2003). https://doi.org/doi:10.1073/pnas.2536313100

44 Balsalobre, A., Damiola, F. & Schibler, U. A Serum Shock Induces Circadian Gene Expression in Mammalian Tissue Culture Cells. *Cell* **93**, 929-937 (1998). https://doi.org/https://doi.org/10.1016/S0092-8674(00)81199-X

45 Bieler, J. *et al.* Robust synchronization of coupled circadian and cell cycle oscillators in single mammalian cells. *Mol Syst Biol* **10**, 739 (2014). https://doi.org/10.15252/msb.20145218

46 Gérard, C. & Goldbeter, A. Entrainment of the Mammalian Cell Cycle by the Circadian Clock: Modeling Two Coupled Cellular Rhythms. *PLOS Computational Biology* **8**, e1002516 (2012). https://doi.org/10.1371/journal.pcbi.1002516

47 Bernard, S., Čajavec Bernard, B., Lévi, F. & Herzel, H. Tumor Growth Rate Determines the Timing of Optimal Chronomodulated Treatment Schedules. *PLOS Computational Biology* **6**, e1000712 (2010). https://doi.org/10.1371/journal.pcbi.1000712

48 Zhu, B. *et al.* A Cell-Autonomous Mammalian 12 hr Clock Coordinates Metabolic and Stress Rhythms. *Cell Metabolism* **25**, 1305-1319.e1309 (2017). https://doi.org/https://doi.org/10.1016/j.cmet.2017.05.004

49 Finger, A.-M. *et al.* Intercellular coupling between peripheral circadian oscillators by TGF-β signaling. *Science Advances* **7**, eabg5174 (2021). https://doi.org/doi:10.1126/sciadv.abg5174

50 Balsalobre, A. *et al.* Resetting of Circadian Time in Peripheral Tissues by Glucocorticoid Signaling. *Science* **289**, 2344-2347 (2000). https://doi.org/10.1126/science.289.5488.2344

51 version 9.11.0.1769968 (R2021b) (The MathWorks Inc., 2021).

52 Leise, T. L. & Harrington, M. E. Wavelet-based time series analysis of circadian rhythms. *J Biol Rhythms* **26**, 454-463 (2011).

53 Lee, G. R., Gommers, R., Waselewski, F., Wohlfahrt, K. & O'Leary, A. PyWavelets: A Python package for wavelet analysis. *Journal of Open Source Software* **4**

54 Myung, J. *et al.* The choroid plexus is an important circadian clock component. *Nature Communications* **9**, 1062 (2018). https://doi.org/10.1038/s41467-018-03507-2

55 Leise, T. L. Wavelet analysis of circadian and ultradian behavioral rhythms. *Journal of Circadian Rhythms* (2013). https://doi.org/10.1186/1740-3391-11-5

56 Barretina, J. *et al.* The Cancer Cell Line Encyclopedia enables predictive modelling of anticancer drug sensitivity. *Nature* **483**, 603-607 (2012). https://doi.org/10.1038/nature11003

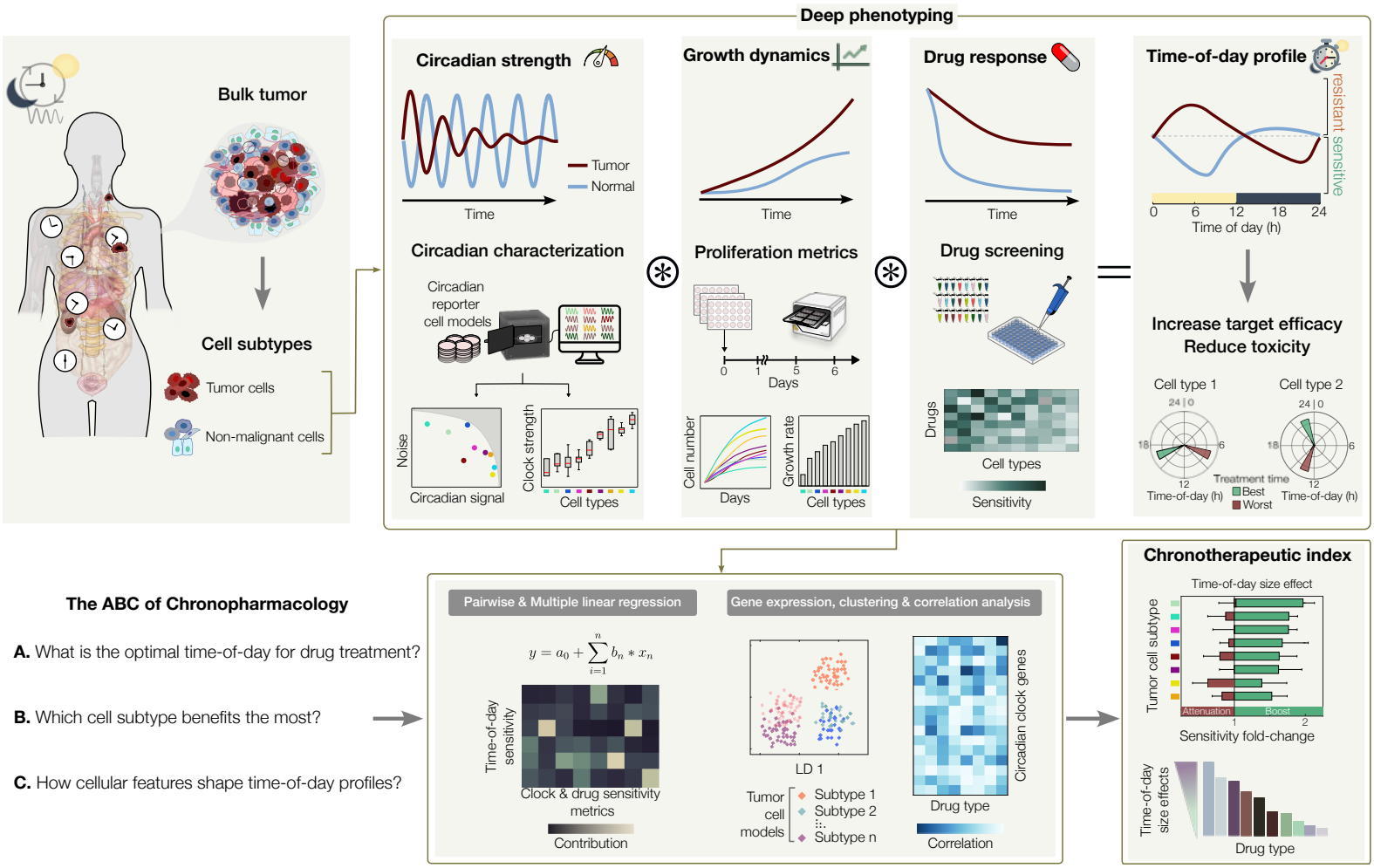

Fig. 1 | Framework for identifying optimal treatment times in cancer and healthy tissue models. Schematic overview of the experimental and computational framework to thoroughly characterize time-of-day drug responses in a variety of cell subtypes, such as cancer and non-malignant cell models. A combination of live recordings is implemented for the deep phenotyping of circadian strength, growth dynamics and drug responses that shape time-of-day profiles. Using a novel streamlined experimental approach, time-of-day sensitivity profiles are obtained in tumor and non-malignant cell models, providing best and worst timings for increased efficacy and reduced toxicity (*top panel*). A tandem computational pipeline integrates the deep phenotyping metrics as well as gene expression data of circadian clock genes to quantitatively address three fundamental questions in chronopharmacology (*bottom panel*). Combining multiple signatures, we define a chronotherapeutic index, ranking cellular models and drug agents by their size-effect gains from drug treatments aligned with the circadian clock (*bottom right panel*).

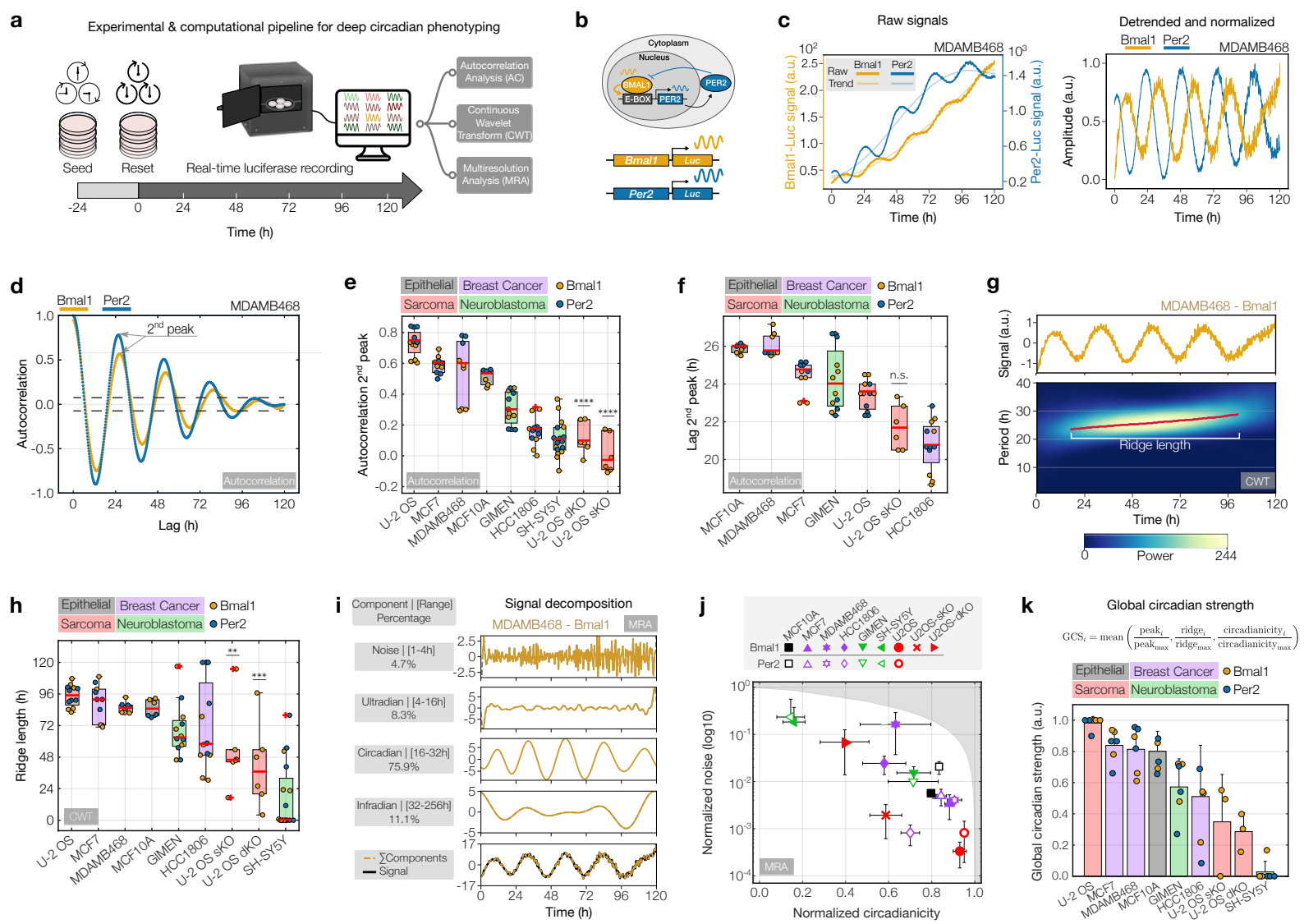

Fig. 2 | Determining circadian clock strength in cancer and healthy tissue cell models. a, Schematic of the experimental setup to detect circadian oscillations. **b,** Circadian feedback loops involving the core clock genes *Bmal1* and *Per2*, used here as circadian Luc-reporters. **c,** Raw (*left*) and processed (*right*) signals from MDAMB468-*Bmal1*/*Per2*-Luc cells. **d,** Autocorrelation (AC) of signals shown in **c**. Arrow indicates 2nd peak and corresponding abscissa (lag). Dashed lines=95% CI. **e,** Boxplot of AC values and **f,** corresponding lags at the 2nd peak of signals from various cell models. **g,** Detrended and amplitude-normalized signal (*top*) and corresponding wavelet power spectrum (*bottom*) obtained from continuous wavelet transform (CWT) showing time-resolved periods of signals from MDAMB468-*Bmal1*-Luc cells. Main oscillatory component (ridge) marked as red line. **h,** Boxplot of CWT ridge lengths of signals from the indicated cell models. Bottom and top edges of the boxes in **e**, **f**, and **h** indicate the 25th and 75th percentiles, respectively. Red horizontal lines denote the data's median and red crosses outliers. *n*=6–17 samples, collected from each reporter cell line. **i,** Multiresolution analysis (MRA) of detrended MDAMB468-*Bmal1*-Luc signals. %=fraction of respective component to total signal. **j,** Scatterplot of normalized noise versus circadianicity of signals from the indicated cell models, determined by MRA. Shaded area covers unattainable range. Data represents the mean±s.d. *n*=3–9 samples per reporter cell line. **k,** Bar diagram ranking cell models by their global circadian strength integrating min-max scaled parameters obtained from AC (peak), CWT (ridge) and MRA (circadianicity) for *Bmal1* and, where applicable, *Per2*. Data represents the mean±s.d of the scaled parameters. For representation purposes, only the positive s.d. is shown. *n*=3–6 input parameters. Color coding of data shown in **b–i** and **k** according to the corresponding Luc-reporter for *Bmal1* (yellow) and *Per2* (blue). Color coding of different cell models in **e**, **f**, **h**, **j**, and **k** according to the tissue of origin. Samples were acquired on two independent days, with each day including 2-3 technical replicates per reporter cell line. MCF10A cells and MDAMB468-*Per2*-Luc cells have been assayed in 3 technical replicates on a single day. One-way ANOVA and Tukey's post-hoc test was applied to compare U-2 OS WT and KO cell lines, where *, **, *** and ****, indicate *p*-values ≤ 0.05, 0.01, 0.001, and 0.0001, respectively. n.s.=non-significant.

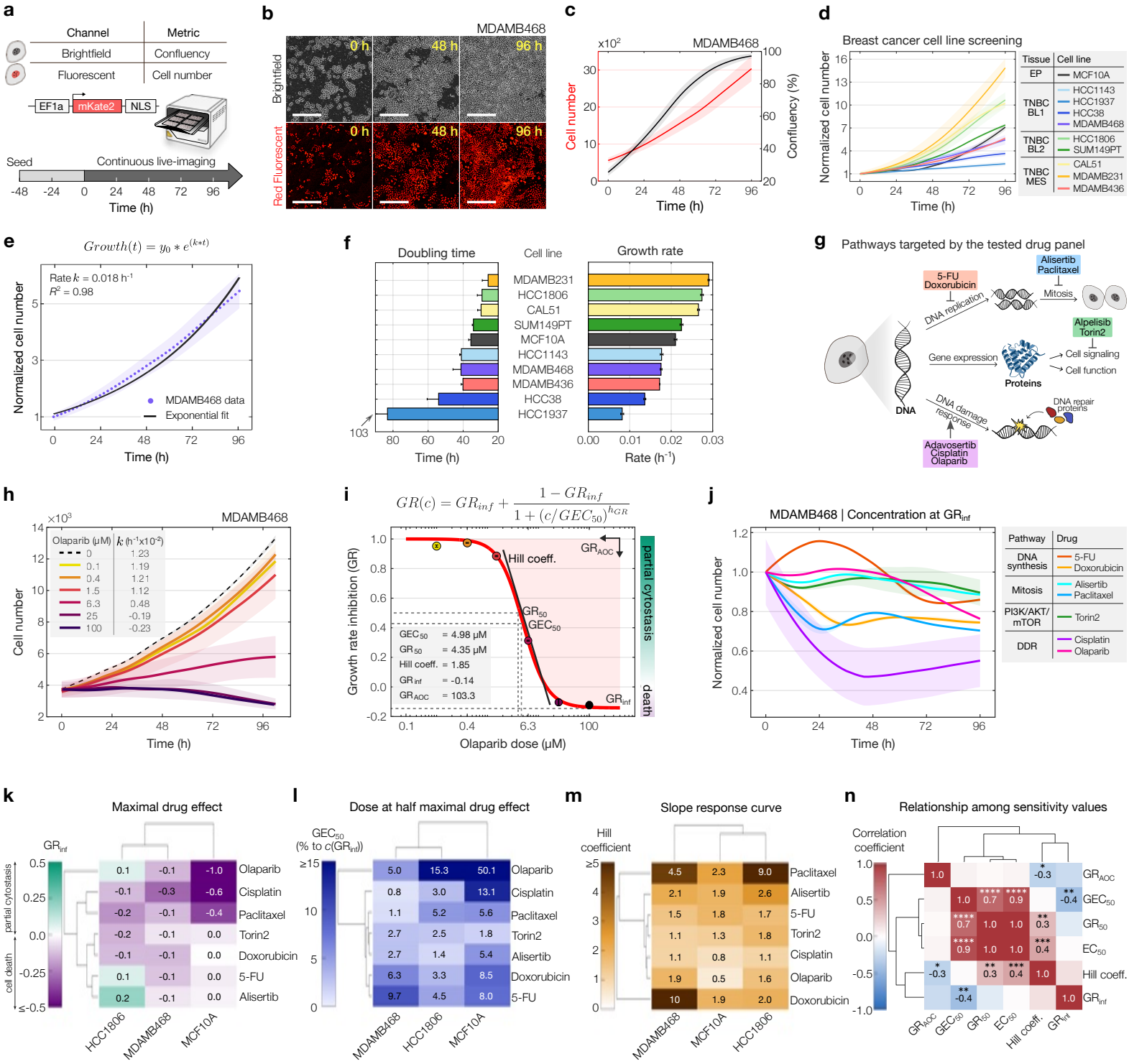

Fig. 3 | Unravelling growth and drug response dynamics through long-term live-cell imaging. a, Schematic of the setup for capturing cell growth using fluorescent nuclear reporters. **b,** Bi-daily snapshots of MDAMB468 cell growth in the brightfield (*top*) and red fluorescent channel (*bottom*). Ruler = 400 μM. **c,** MDAMB468 confluency (*black line*) and cell numbers (*red line*) over time. **d,** Normalized growth curves of the indicated cell models. BL1, BL2 and MES refer to the TNBC subtypes basal-like 1, basal-like 2, and mesenchymal-like, respectively. EP is short for for epithelial. **e,** Exponential fit (blacl solid line) for MDAMB468 growth curves, yielding the growth rate (*k*), and fit accuracy (R^2). The dots represent mean normalized cell numbers calculated from two independent assay plates, the shaded area represents the corresponding standard deviation. **f,** Bar diagrams ranking cell models by doubling times and growth rates. Data in **c–f** represents the mean ± s.e.m. from 9 images taken per cell line on a single plate. *k*-value errors reflect the 95% CI. For clarity in **f**, one-sided error bars are shown, with the arrow indicating the top range of the respective error bar. **g,** Schematic of the pathways targeted by the drugs used in this study. **h,** Cell numbers and corresponding *k*-values of MDAMB468 cells treated with varying olaparib doses (color-coded) or solvent (dashed line). Data represents the mean ± s.d. of two plates. **i,** Dose-response curve of *GR* values corresponding to **h**, highlighting various drug sensitivity metrics. Error bars = 95% CI. **j,** Normalized numbers of MDAMB468 cells treated with the GR_{inf} dose of the indicated drugs. Data represents the mean ± s.d. of two plates, or ± s.e.m of 9 images taken per cell line on a single plate (cisplatin). **k–m,** Hierarchical clustering of drug sensitivity parameters across cell-drug combinations. GEC_{50} values in **l** are shown relative to the GR_{inf} dose. **n,** Pearson's linear correlation coefficients of sensitivity parameters shown in **k–m** and additional cell-drug combinations (see Supplementary Table 1; *n*=49–50). Denoted are significant correlation coefficients, where *, **, ***, and **** indicate *p*-values ≤ 0.05, 0.01, 0.001, and 0.0001, respectively. Data in **k–n** based on the mean of two plates or 9 images taken per well on a single plate (cisplatin).

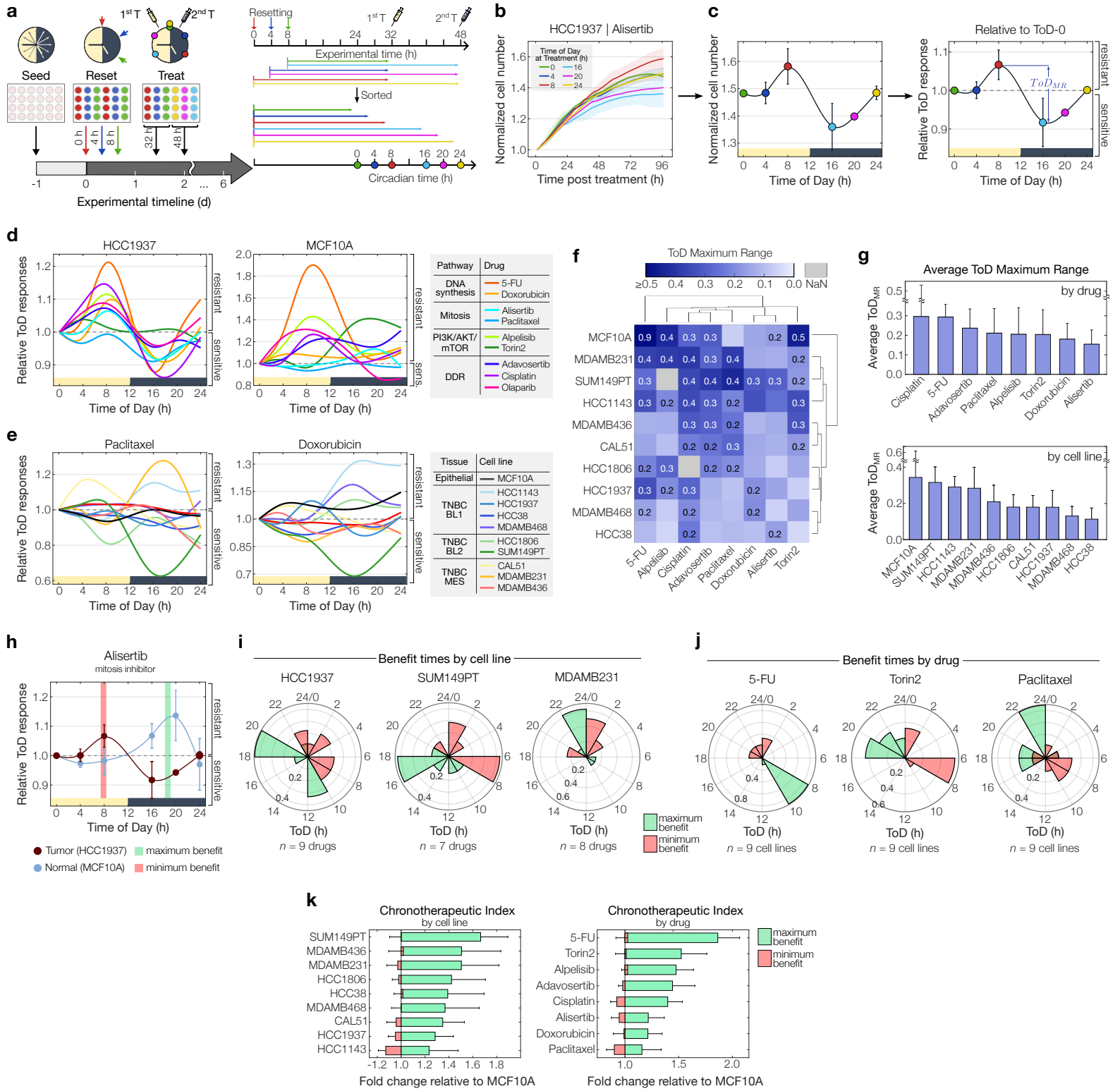

Fig. 4 | Time-of-day drug sensitivity is drug and tissue model dependent. a, Schematic of the experimental setup to screen for time-of-day (ToD) responses. Three clock-resetting steps are performed in 4-h intervals. Drugs are administered 32 or 48 h post-initial reset, resulting in six circadian times (0, 4, 8, 16, 20 and 24 h). Growth is monitored by long-term live-cell imaging. Timelines on the right depict experimental (*top*) and relative circadian times (*bottom*), color-coded by each ToD tested. **b,** Cell counts of HCC1937 treated with alisertib at different times of the day. Normalization to respective time of treatment. **c,** Cell numbers 4 days post-treatment versus treatment times, corresponding to **b** (*left*). ToD response curve (ToD-RC) depicting relative responses to ToD 0 h. Blue arrows mark the maximum ToD response range (ToD_{MR}) (*right*). **d,** ToD-RCs for HCC1937 (*left*) or MCF10A (*right*) cells treated with different drugs (color-coded). **e,** ToD-RCs for 10 cell models treated with paclitaxel (*left*) or doxorubicin (*right*). Color coding of cell models according to tissue of origin. **f,** Hierarchical clustering of ToD_{MR} values across drug-cell combinations. Values above 0.2 are shown. Data clustering with the UPGMA method and euclidian distance. **g,** Bar diagrams ranking ToD_{MR} values per drug (*top*) and cell model (*bottom*). **h,** ToD-RCs for alisertib-treated HCC1937 tumor and MCF10A non-tumor cells overlaid, yielding maximum and minimum benefit times. Data shown in **b–h** represents mean (± s.d.) of two plates. **i,** Polar histograms for benefit times across cell models (*n*=7–9 drugs) and **j**, drugs (*n*=9 cell models). **k,** Butterfly charts depicting fold changes relative to MCF10A at benefit times, averaged per cancer cell model (*left*) and drug (*right*). Color-coding of maximum and minimum benefit times shown in **h–k** in green and red, respectively. Data shown in **g** and **k** represents mean ± s.d. of tested cell models per drug and vice versa (*see* **f**). For clarity, one-sided error bars are shown.

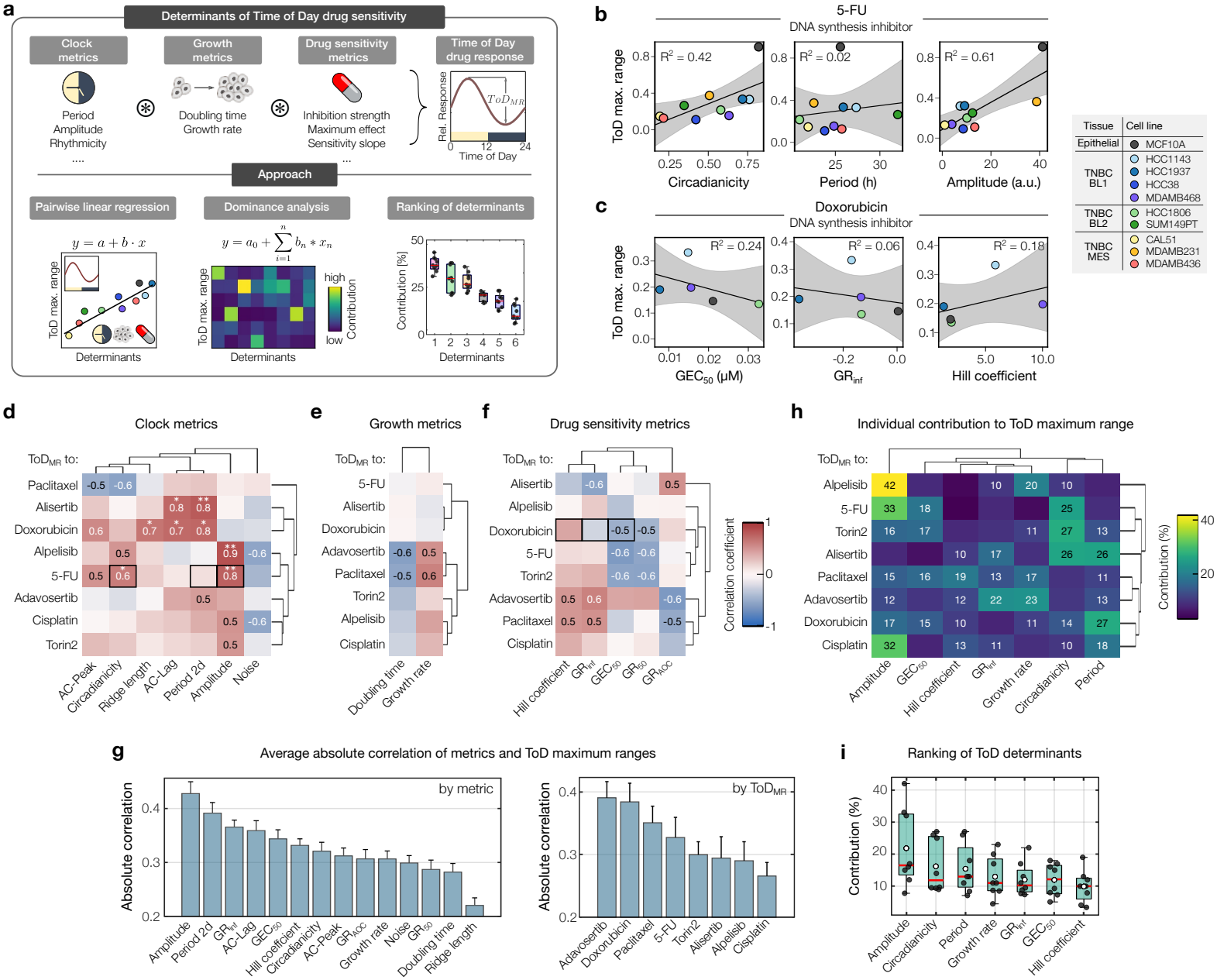

Fig. 5 | Clock and drug sensitivity metrics shape ToD curves. a, Computational approach to investigate how circadian rhythms, cell growth dynamics, and drug sensitivity factors influence the time-of-day (ToD) drug efficacy. **b,** and **c,** Example of linear correlations between $_{MR}$ and circadian (**b**) or drug sensitivity parameters (**c**), for 5-FU (n=10 cell models) and cisplatin (n=5 cell models), respectively. Color coding of cell models according to tissue of origin. Grey-shaded area=95% CI. Model accuracy indicated by R^2-values. **d–f**, Hierarchical clustering of correlation coefficients (r) between ToD_{MR} values of different drugs (*rows*) and the respective metric (*columns*) for clock strength (**d**, n=10 cell models), growth (**e**, n=10 cell models) or drug sensitivity (**f**, n=5 cell models). r-values ≥ 0.5 and ≤ -0.5 are shown. Black boxes indicate examples shown in **b** and **c**. Statistical significance of pairwise correlations is indicated by stars, where *, and **, denote p-values ≤ 0.05 and 0.01, respectively. *Note*: sample size in **d–f** for alpelisib=n-1; and for cisplatin=9. **g,** Bar diagrams ranking the absolute correlation between ToD_{MR} values and each metric depicted in **d–f**, ranked by metric (n=8 drugs) or by drug (n=14 metrics). Data represents the mean ± s.e.m. For clarity, one-sided error bars are shown. **h,** Hierarchical clustering of the dominance analysis matrix showing the individual contribution of circadian clock, growth and drug sensitivity parameters (*columns*) in predicting drug dependent ToD_{MR} values (*rows*). Colors indicate the percentage contribution, as detailed in the color bar. See key for **d–f** for sample sizes (n). **i,** Boxplot of overall contribution of cellular metrics to predict ToD_{MR} values, corresponding to **h**. Black data points indicate the individual result from each drug (n=8 drugs). Red horizontal lines denote the median, white circles denote the mean. Bottom and top edges of the boxes indicate the 25th and 75th percentiles, respectively.

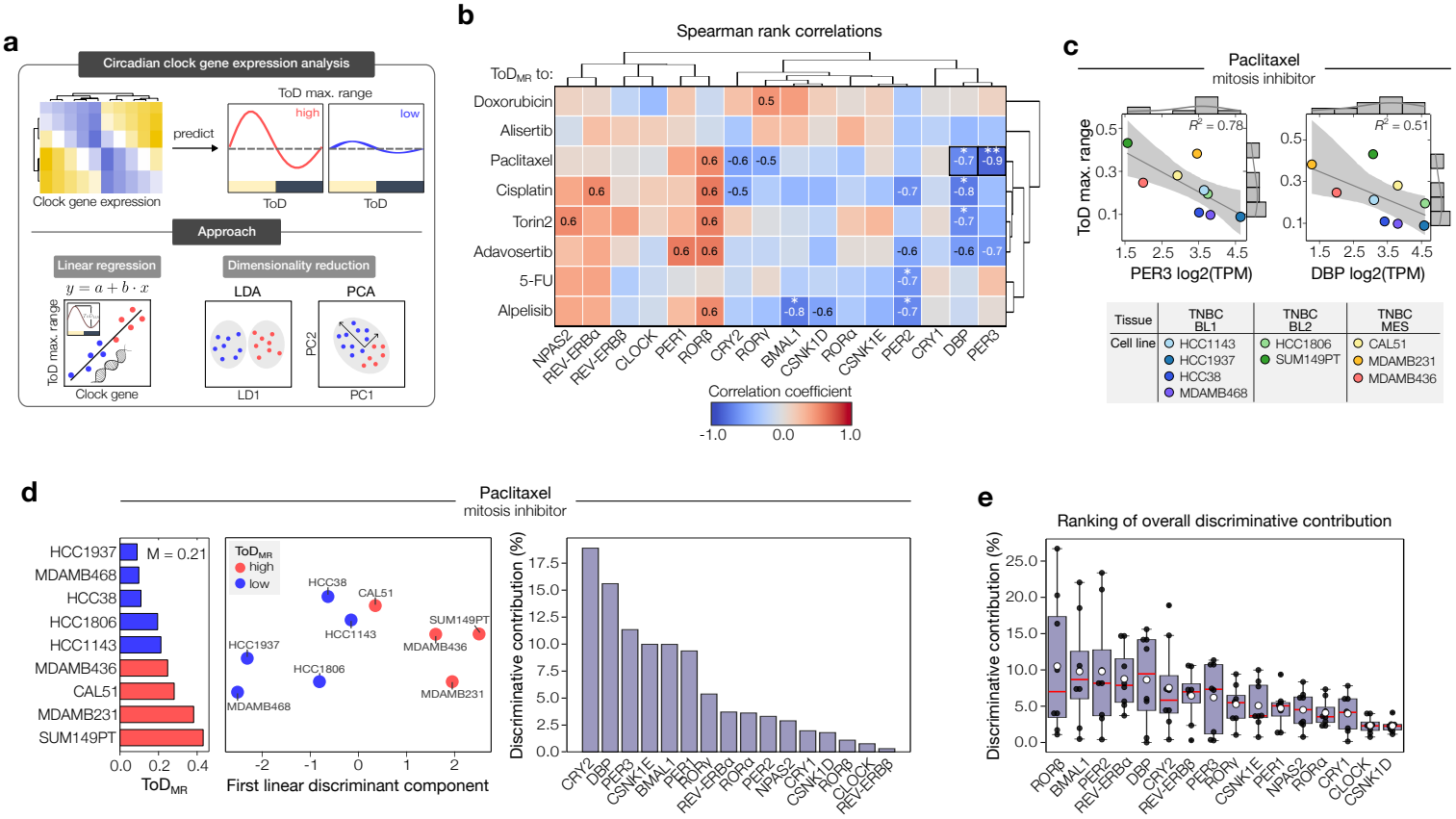

Fig. 6 | Gene expression analysis unveils diverse roles of circadian genes in determining time-of-day patterns. a, Approach to identify the role of core clock genes in determining the strength of time-of-day (ToD) drug sensitivity. **b,** Hierarchical clustering of spearman rank correlation coefficients between drug-dependent *ToD*$_{MR}$ values (*rows*) and core clock genes (*columns*). Black boxes indicate examples shown in **c**. Statistical significance of the correlations are indicated as stars, where * and **, denote *p*-values ≤ 0.05 and 0.01, respectively. Cisplatin and alpelisib: *n*=8 cell lines, else *n*=9 cell lines. **c,** Example of linear correlation analysis between paclitaxel *ToD*$_{MR}$ values and *Per3* or *Dbp* expression levels measured as log2(TPM). Color-coded data points indicate different cancer cell models. Grey-shaded area=95% CI. Model accuracy indicated by R^2-values. Top and lateral histograms indicate the count of samples along the range of gene expression, and *ToD*$_{MR}$ values, respectively. The grey continuous line indicates the normal distribution fit of the samples. *n*=9 cell lines. **d,** Linear discriminant analysis (LDA) on median-based binarized *ToD*$_{MR}$ values for paclitaxel. Cell models with *ToD*$_{MR}$ values below or above the median (M) are colored in blue and red, respectively (*middle and left panel*). The contribution to the obtained discriminative information is shown in percentage for each of the circadian clock genes (*right panel*). **e,** Boxplot showing the mean-based ranking of overall discriminative contributions of each circadian clock gene across all tested drugs. *n*=8 drugs. Bottom and top edges of the boxes indicate the 25th and 75th percentiles, respectively. Red horizontal lines denote the median, white circles the mean, and red crosses indicate outliers.

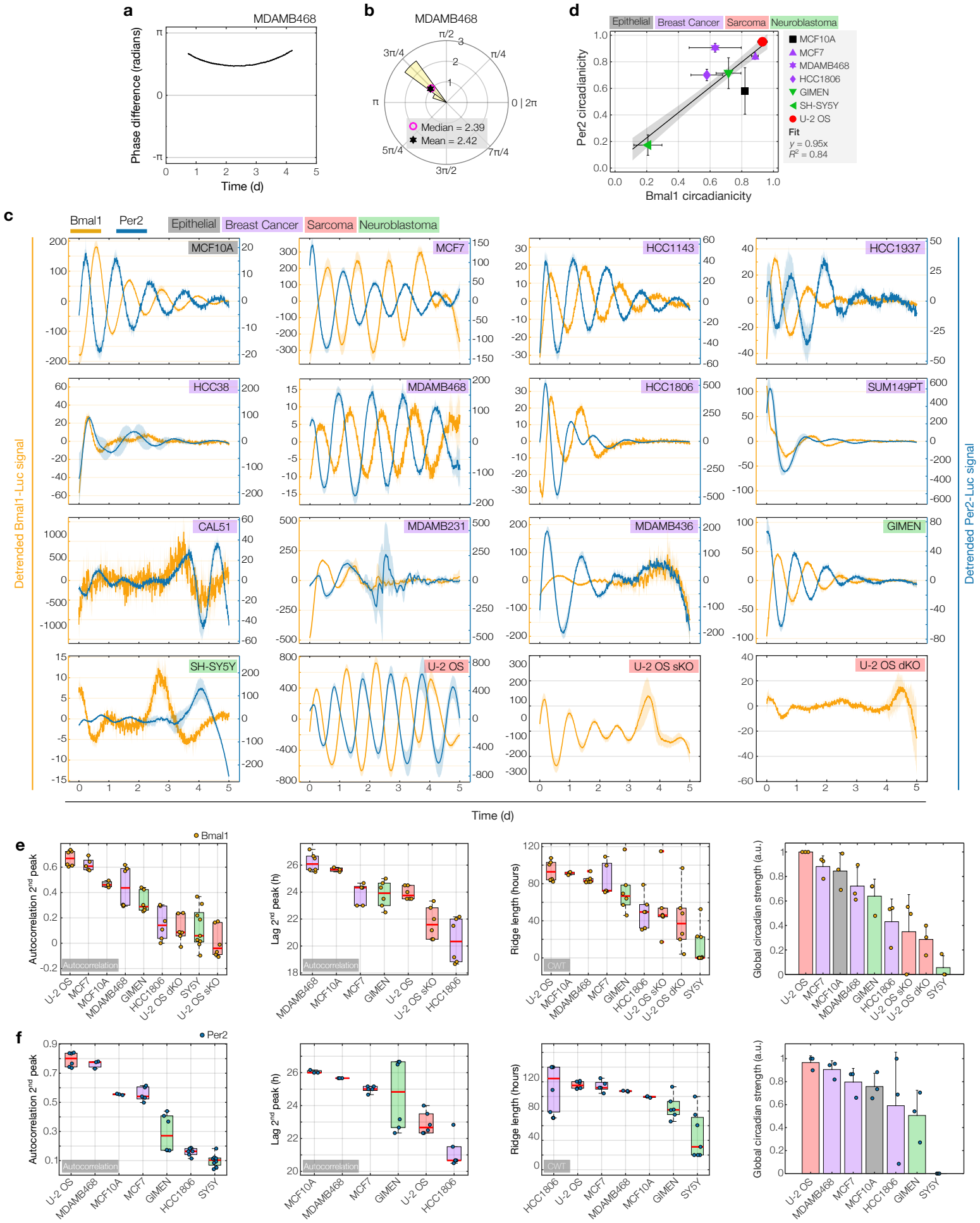

Supplementary Fig. 1. a, Example of absolute phase difference evolution between *Bmal1*- and *Per2*-Luc signals, here shown for single samples of MDAMB468 cells. **b,** Polar histogram depicting the phase difference between *Bmal1* and *Per2* signals in MDAMB468 cells over time. 2π denotes one full circadian cycle. Median and mean phase difference are indicated as pink circle and black star, respectively. **c,** Detrended *Bmal1*- (*yellow*) and *Per2*-Luc (*blue*) signals of all cell lines used in this study. Data represents the mean±s.d. of 3 technical replicates recorded on the same day. **d,** Linear regression analysis of the MRA circadian component ('circadianicity') of *Bmal1*- versus *Per2*-Luc signals. Markers indicate different cell models. Grey-shaded area=95% CI. Model accuracy indicated by R^2-values. Data represents the mean±s.d. of 3–9 samples. **e,** *Bmal1*- and **f,** *Per2*-dependent circadian analysis corresponding to the rankings of the combined data shown **Fig. 2e, f, h, k**. Bottom and top edges of the boxes in the box plots indicate the 25th and 75th percentiles, respectively. Red horizontal lines denote the data's median and red crosses outliers. *n*=3–9 samples. Color-coding of cell models in **c-f** according to their tissue of origin. Samples in **d-f** were acquired on two independent days, with each day including 2-3 technical replicates per reporter cell line. MCF10A cells and MDAMB468-*Per2*-Luc cells have been assayed in 3 technical replicates on a single day.

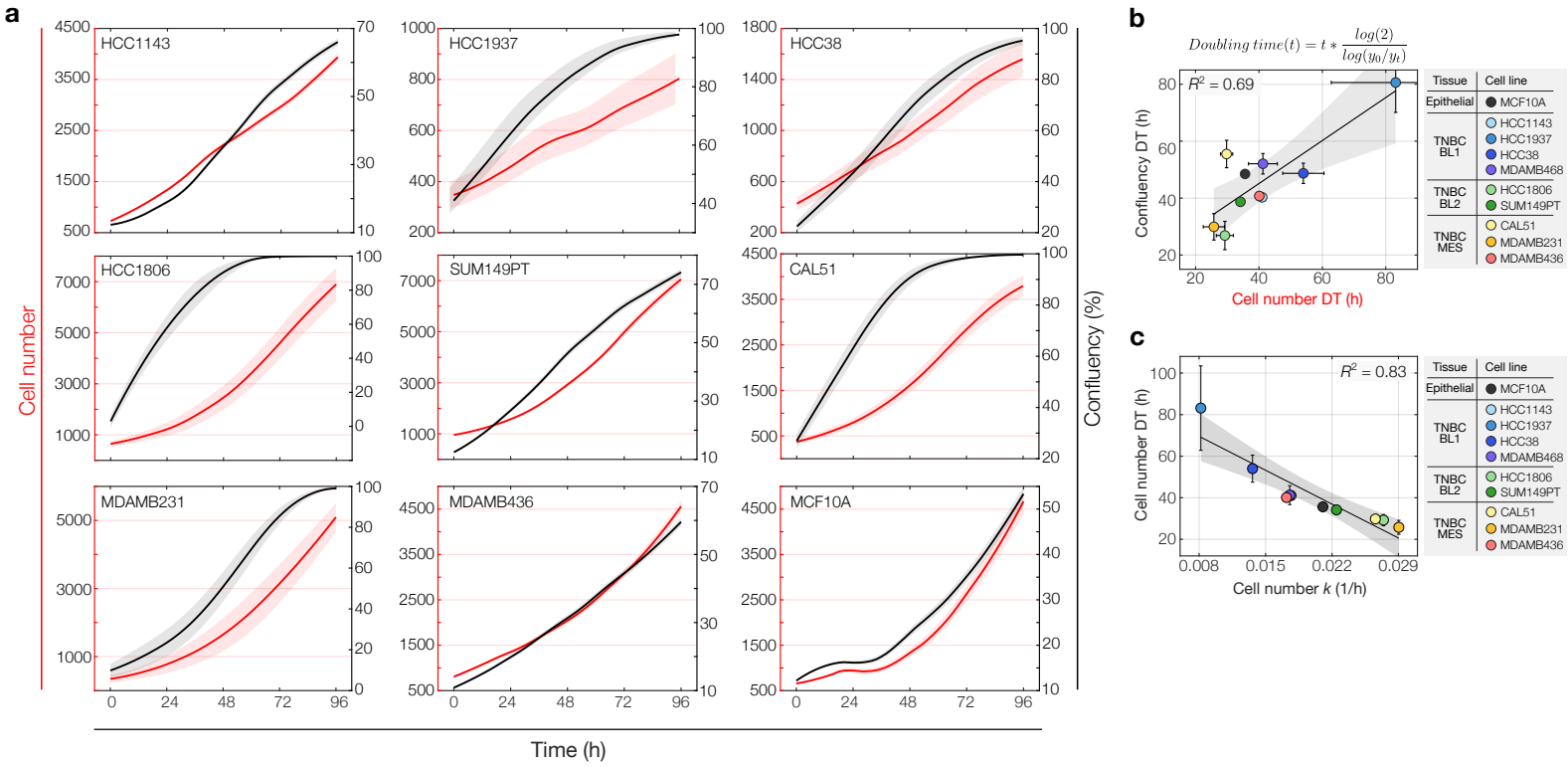

Supplementary Fig. 2. a, Growth curves of the indicated cell lines monitored by live-cell imaging for 4 days and quantified by either cell numbers (*red line*) or confluency (*black line*). Data represents the mean±s.e.m. of 9 images taken per cell line on a single plate . **b,** Linear regression analysis of doubling times (DT's) calculated from confluency versus cell numbers. **c,** Linear regression analysis of the doubling time and growth rate (*k*) calculated from cell numbers of various cell lines. Color coding of cell models in **b** and **c** according to their tissue of origin. Data shown in **b** and **c** represents the mean±s.d. (DT's), or ±CI of the exponential fit (*k*-values). Grey-shaded area=95% CI. Model accuracy indicated by R^2-values.

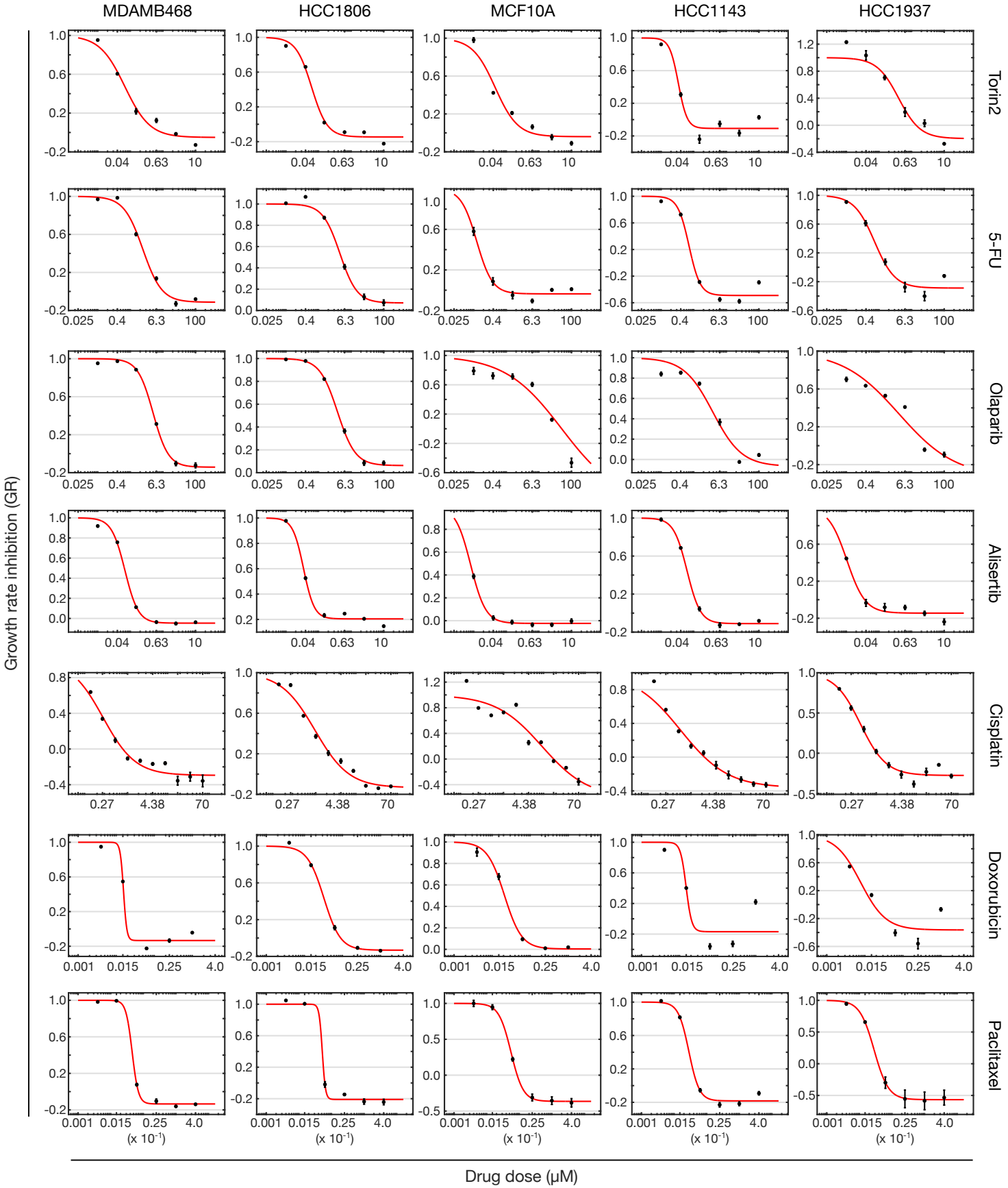

Supplementary Fig. 3. Dose-response curves of *GR* values for the specified cell models and drugs. The data is based on the mean responses of technical replicates, live-imaged on independent assay plates for 4 days. For cisplatin, 9 images were taken per cell line on a single plate. Error bars indicate the 95% CI of the exponential fit.

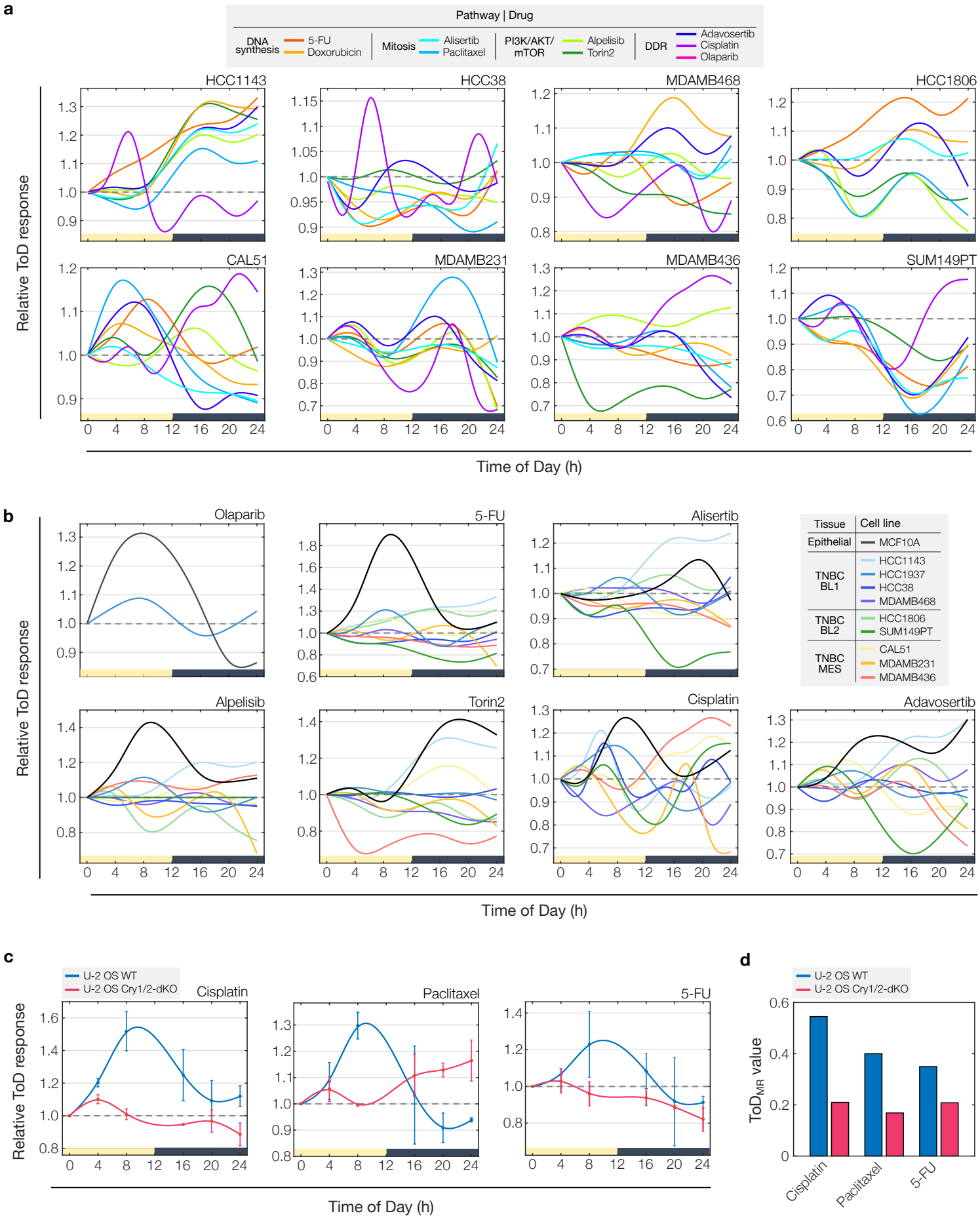

Supplementary Fig. 4. a, Overlay of ToD response curves (ToD-RCs) for individual cell models treated with different drugs (color-coded). **b,** Overlay of ToD-RCs for multiple cell models, grouped by the administered drugs. Cell line models are color-coded. Data in **a** and **b** represents the mean for each drug-cell combination tested on two plates or 9 images (cisplatin). **c**, Overlay of ToD-RCs for U-2 OS wildtype and circadian *Cry1*/*Cry2*-double knock-out cell lines, grouped by the administered drugs. Cell line models are color-coded. Data represents the mean (± s.d.) of two plates. **d**, Ranking of ToD$_{MR}$ values for each drug-cell combination.

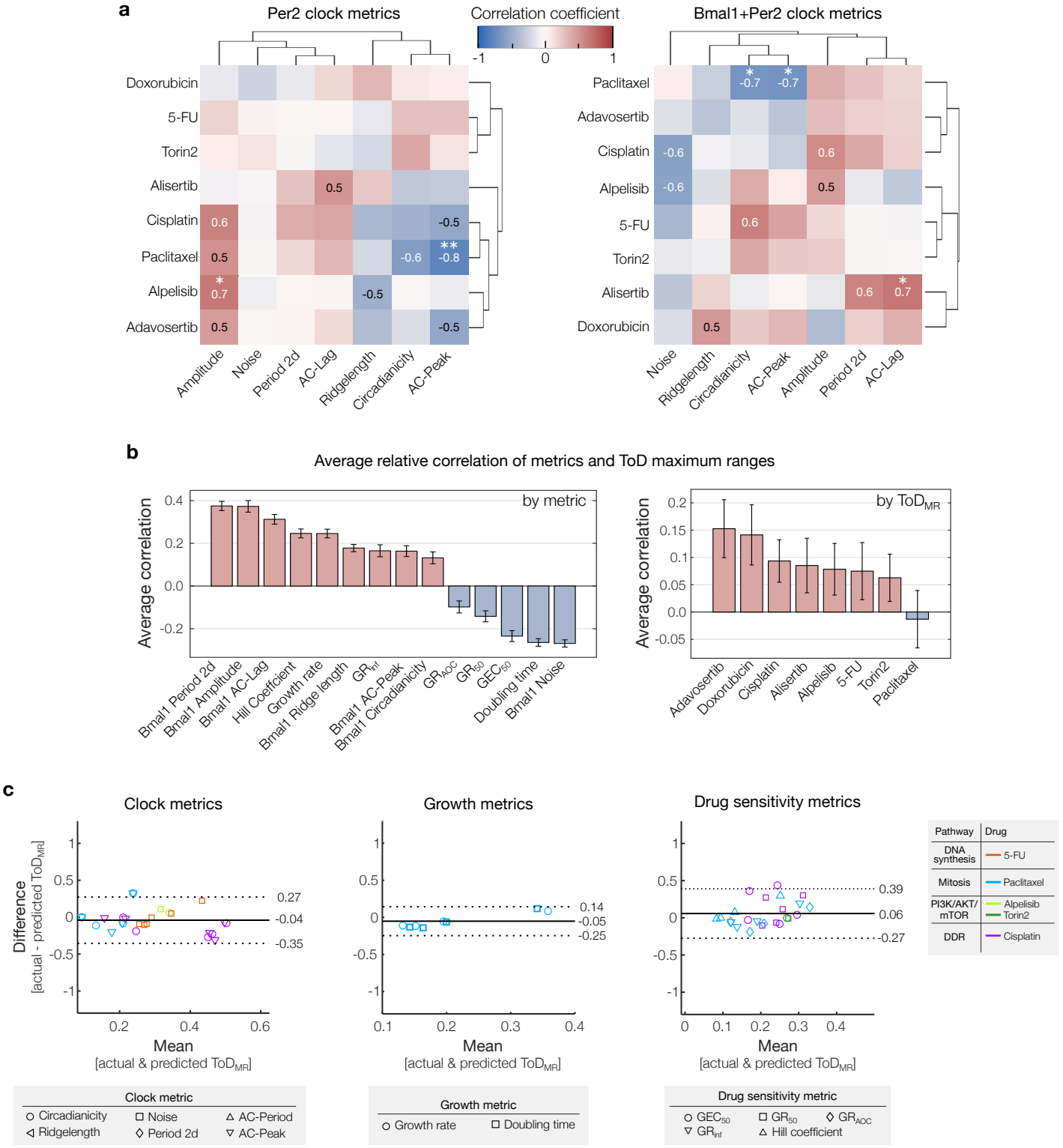

Supplementary Fig. 5. a, Hierarchical clustering of correlation coefficients between ToD_{MR} values for different drugs (*rows*) and clock strength metrics (*columns*) obtained from the *Per2*-reporter (*left*) or calculated as a mean from both, *Bmal1*- and *Per2*-reporters (*right*). Statistical significance of pairwise correlations is indicated by stars, where * and **, denote *p*-values ≤ 0.05 and 0.01, respectively. *n*=10 or 9 (cisplatin and alpelisib) cell models. **b,** Bar plots ranking relative overall correlation between ToD_{MR} values and individual cellular metrics (depicted in **Fig. 5d–f**), averaged by metric (*left*, *n*=8 drugs) or by drug (*right*, *n*=14 metrics). Positive and negative correlation values are color-coded in light red and blue, respectively. Data represents the mean±s.e.m. **c,** Bland-Altman plots comparing predicted and actual ToD_{MR} values of new data that was not used to derive the original statistical associations shown in **Fig 5d-f**, including 26, 8, and 24 new datapoints for the clock, growth, and drug sensivity datasets, respectively (refer to **Supplementary Table 3** for full new datatset). The predictions were based on fitting a linear regression model to the original data associated with pearson correlation coefficients ≥ 0.5. The individual parameters considered for each dataset are distinguished by marker, different drugs are uniformly color-coded across all three datasets. The central solid line indicates the mean bias between the predicted and actual ToD_{MR} values of the new data and the outer lines mark the upper and lowers limits of agreement (±1.96*s.d.).

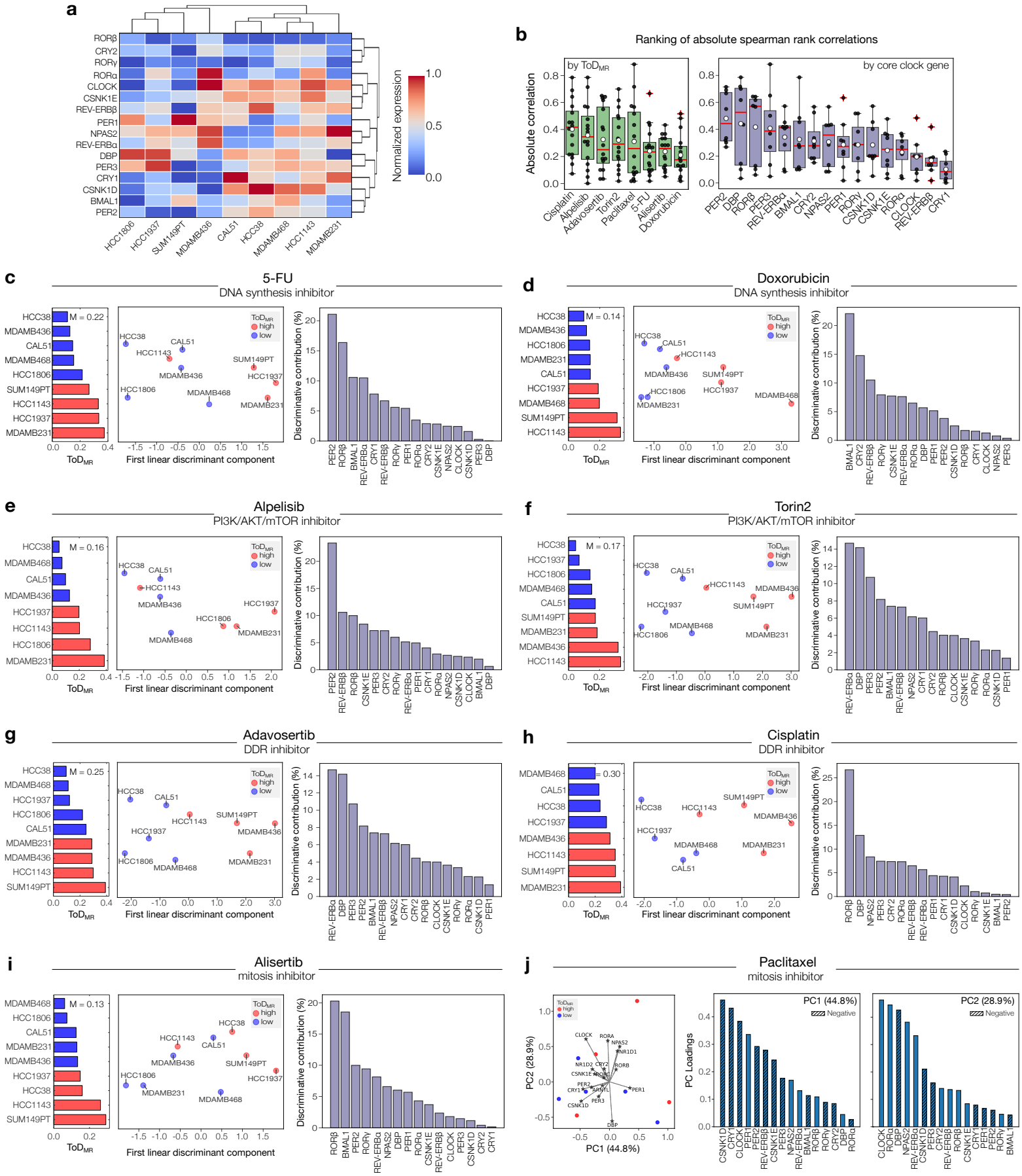

Supplementary Fig. 6. a, Gene expression clustermap of the selected list of core clock genes (*rows*) for the different cell models (*columns*) used in this work. **b,** Boxplot showing the mean-based ranking of absolute spearman rank correlation values between circadian clock gene expression levels and ToD_{MR} values, categorized by drug (n=16 circadian clock genes) or by circadian clock gene (n=8 drugs). Bottom and top edges of the boxes indicate the 25th and 75th percentiles, respectively. Red horizontal lines denote the median, white circles the mean, and red crosses indicate outliers. **c-i,** Linear discriminant analysis on median-based binarized ToD_{MR} values for the indicated drugs. ToD_{MR} values below or above the median (M) are color-coded as blue and red, respectively (*middle and left panel of each subfigure*). The contribution to the obtained discriminative information is shown in percentage for each of the circadian clock genes (*right panel of each subfigure*). **j,** Principal Component Analysis (PCA) biplot of the first two principal components on ToD sensitivity groups related to paclitaxel, with ToD sensitivity groups color-coded. Overlaid are the principal component scores for circadian clock genes, scaled to demonstrate their relative contribution to determining ToD sensitivity. The percentage of variance explained by each principal component is denoted by their respective loadings (*left panel*). The bar charts detail the ranked contribution of individual circadian clock genes to PC1 and PC2, presented in descending order (*middle and right panels, respectively*).

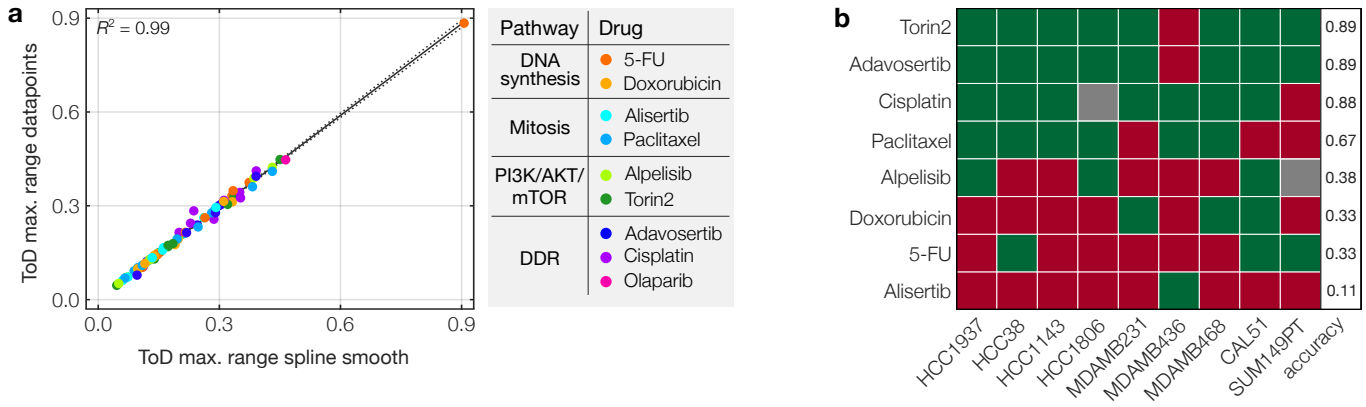

Supplementary Fig. 7. a, Linear regression analysis of the maximum range in ToD responses (ToD_{MR}), determined from the discrete measured data points or from continuous spline smoothed ToD response curves. Drugs are color-coded. Dotted lines=95% CI. Model accuracy indicated by R^2-values. *n*=80 drug-cell combinations. **b,** Leave-one-out cross-validation test (LOOCV) on LDA results shown in **Fig. 6d** and **Supplementary Fig. 6d-h**, where the potential of circadian gene expression levels to discriminate between high and low ToD sensitivity groups (based on median-binarized ToD_{MR} values) is investigated. The color coding reflects the accuracy of each cell line model in being correctly assigned to its ToD-sensitivity group, where green and red indicate true and false categorization, respectively. The rightmost column denotes the summed LOOCV accuracy per drug, where 1 refers to 100% accuracy and 0 to 0%. *n*=9 cell line models; cisplatin and alpelisib: *n*=8 cell line models.